

Design and kinematic analysis of the novel almost spherical parallel mechanism Active Ankle

Shivesh Kumar · Bertold Bongardt · Marc Simnofske · Frank Kirchner

Received: date / Accepted: date

Abstract The novel mechanism ACTIVE ANKLE features three degrees of freedom that operate in an almost spherical manner. In comparison to spherical devices, its design offers advantages such as high stiffness, a simple and robust construction, and a good stress distribution. In the present paper, a comprehensive study of the design, analysis, and control of the ACTIVE ANKLE in its almost-spherical work modality is provided. In particular, the kinematic analysis of the mechanism is conducted, solving the full inverse, the rotative inverse, and the forward kinematic problems. In addition, the manipulator's workspace is characterized and the kinematic control, that has been implemented on a prototype of ACTIVE ANKLE, is presented together with experimental results that demonstrate the employability as an ankle joint in a full body exoskeleton.

Keywords Parallel Robots, Kinematics, Mechanism Design of Manipulators, Prosthetics and Exoskeletons.

Acknowledgements The work presented in this paper was performed within the project *Recupera-Reha*, funded by the German Aero-space Center (DLR) with federal funds from the Federal Ministry of Education and Research (BMBF) (Grant *01-IM-14006A*).

S. Kumar, M. Simnofske, F. Kirchner
Robotics Innovation Center (RIC), German Research Center for Artificial Intelligence (DFKI), 28359 Bremen, Germany
E-mail: shivesh.kumar@dfki.de, marc.simnofske@dfki.de, frank.kirchner@dfki.de

B. Bongardt
Institute of Robotics and Process Control (IRP), Technical University of Braunschweig, 38106 Braunschweig, Germany
E-mail: b.bongardt@tu-bs.de

1 Introduction

A parallel manipulator (PM) is defined as a closed-loop mechanism in which the end effector (the mobile platform) is connected to the base by at least two kinematic chains [28]. The DELTA robot [9] and its variants [7] probably represent the most successful class of parallel manipulators employed in industry. On the contrary, an end effector in serial manipulators is connected to the base by a single series of links and joints. In comparison to a serial mechanism, a parallel mechanism generally offers higher stiffness, speed, accuracy, and payload capacity, at the downside of a reduced workspace and a complex geometry that needs careful analysis and control [23, 28].

If the location of a point on the end-effector's lamina [10] of a PM remains constant, the device is called a spherical parallel manipulator (SPM). The AGILE EYE [15] and its improved variant AGILE WRIST [31] are prominent examples of SPMs with three degrees of freedom (DOF). The joint axes of this class of spherical manipulators are required to intersect in a single point. However, due to machining and assembling errors, it is difficult to achieve an accurate intersection of all joint axes [13]. Misalignments may lead to undesirable reaction forces in the structure, and hence to a reduced service life of the mechanism or sometimes makes the complete system difficult to assemble [41]. Moreover, the use of C-shaped links in the system prevents the design from being used in high payload applications. Due to the kinematic layout that requires an exact intersection of all rotation axes, a high-precision manufacturing is indispensable for these SPMs [1]. The ARGOS mechanism, an SPM with three DOF, was developed by Vischer and Clavel [41] to overcome these shortcomings. Their 3[$R[RR/SS]S$]-design consists of three identical



Fig. 1: A built-up prototype of the 3-DOF ACTIVE ANKLE incorporating actuators and control electronics. Its technical specifications are outlined in Section 2.2.

legs containing a revolute joint at the base whose axis is pointing to a virtual rotation center.

The novel, almost-spherical parallel manipulator ACTIVE ANKLE (Figure 1) has recently been introduced in [35]. Due to its unique, simple and compact $3[R2][SS]$ design, the constraint of moving the end effector about an exact center (of rotation) in case of SPMs is relaxed to almost spherical motions that includes a translational shift of the end effector about a tolerated, very small domain. The motivation for the development of the novel mechanism as an ankle joint of a full-body exoskeleton has been provided in [35], together with a comparison to other SPMs [39, 40, 44]. Further its type synthesis, design, construction, and simulation results have been laid out [35].¹ Additionally, insights into the principal solvability of the forward kinematics problem of the ACTIVE ANKLE and its different assembly modes have been obtained [24]. The real, almost-spherical assembly mode still needs a careful analysis to enable for practical applications and systematic design modifications. Due to the spatial behavior but spherical use case of the ACTIVE ANKLE, the understanding and modeling of its geometry is a challenging and interesting problem. Its solution provides a basis for a kinematic control strategy as a spherical device.

Contributions. In the present paper, a comprehensive study of the design, analysis, and control of the ACTIVE ANKLE in its almost-spherical work modality is provided. First, the combinatoric and geometric type of the parallel mechanism is set into context of the state-of-the-art. Crucial features of its design and construction

¹ Further similar designs – involving three legs and a quadrilateral loop – are the translative $3[R2][RR]RR$ -device [26] and the spatial $3[2][UPR]U$ -manipulator [27].

are pointed out. Second, the definitions of the inverse kinematic problems associated to the mechanism and suitable solution methods including all required sub-routines are presented explicitly. In particular, this includes the extension of the inverse kinematic problem to the rotative inverse kinematic problem.² The solution to the latter – that asks for a joint configuration for a given orientation from $SO(3)$, instead of a pose from $SE(3)$ – is provided in the form of a novel iterative approach that can be described by the concept of virtual joints [3, 6, 8]. The auxiliary output of this solution also provides a quantification to the extent of parasitic translative motion of the mechanism. Third, the workspace of the ACTIVE ANKLE in its almost-spherical assembly mode is characterized in detail. This includes the consideration of the primary rotative and the secondary translative domains of the workspace. The physically realizable boundaries are studied with respect to constraints imposed by principal link intersections and by limits of employed spherical joints. Fourth, the applicability of the device and the elaborated solution methods of its inverse problems are demonstrated in a range of motion analysis and in control experiments, both in accordance with the human ankle joint.

As a side contribution, the paper contains the formulation of a novel algorithm for computing the intersection points of three spheres by using the concept of Cayley–Menger bideterminants. The method is called as a subroutine during the computation of the translative endeffector shift for given input angles and platform orientation. Overall, the present paper answers the most crucial and practical questions arising in the analysis, the control, and the employment of the ACTIVE ANKLE as an almost-spherical device.

Notation. For the notation, a few conventions are introduced in accordance to [5]. The dot \cdot is used to indicate matrix-matrix, scalar-matrix, and scalar-scalar multiplications. The inner product of a vector $\mathbf{a} = (a_1, a_2, a_3)^T$ and a vector $\mathbf{b} = (b_1, b_2, b_3)^T$ is denoted as $\mathbf{a} * \mathbf{b} = \sum_i a_i \cdot b_i$. The expression \mathbf{a}^\otimes describes the skew-symmetric matrix, $\mathbf{a}^\otimes = \begin{pmatrix} 0 & -a_3 & a_2 \\ a_3 & 0 & -a_1 \\ -a_2 & a_1 & 0 \end{pmatrix} = \mathbf{S}$, the ‘cross matrix’ associated to a vector \mathbf{a} . In the opposite direction, the vector is extracted as $\mathbf{S}^\oplus = \mathbf{a}$. A vector of length one is indicated with a hat, as $\hat{\mathbf{a}}$ (so that $\|\hat{\mathbf{a}}\|^2 = \hat{\mathbf{a}} * \hat{\mathbf{a}} = 1$). As an operator, \mathbf{a}^\odot normalizes as $\odot : \mathbf{a} \mapsto \hat{\mathbf{a}} = \frac{\mathbf{a}}{\|\mathbf{a}\|}$. The matrix $\mathbf{M}^{\circ\frac{1}{2}}$ contains the roots of the elements of a matrix \mathbf{M} (Hadamard root).

² Within this paper, the term ‘kinematic problem’ is exclusively used for a ‘finite kinematic problem’. Such problem is also qualified as ‘geometric’ (in contrast to ‘instantaneous kinematic’) by other authors [11, 20, 43].

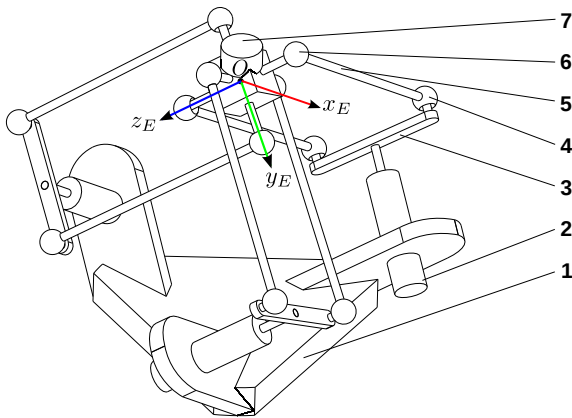


Fig. 2: Sketch of the ACTIVE ANKLE [34] including (1) base, (2) rotative actuator, (3) crank, (4 & 6) ball and socket joints, (5) rod, (7) end-effector.

Structure. The paper is organized as follows: In Section 2, the design and the construction of the ACTIVE ANKLE are reflected in comparison to the state-of-the-art and its general mobility is determined. In Section 3, the inverse kinematic problems and solution methods suitable for its kinematic control are presented. In Section 4, a numerical forward kinematic analysis is presented together with a characterization of the mechanism's workspace. The Section 5 presents the control of the ACTIVE ANKLE in comparison to the range of motion of the human ankle. Finally, conclusions are drawn in Section 6.

2 Design and Topology

2.1 Type Synthesis

The combinatoric and geometric type of the spatial almost-spherical parallel mechanism ACTIVE ANKLE are set into context in Table 1 and Table 2. With a homogeneous distribution of five DOF to all three legs (Table 1), the combinatorics of the ACTIVE ANKLE matches those of the DELTA robot. The topological setup of both mechanisms also equals on the level of each of the three identical legs: Both consist of one rotative actuator in series with one closed loop with four spherical joints (Figure 3). For these reasons, the ACTIVE ANKLE can be classified as the (almost) rotative counterpart of the DELTA robot. In comparison to the DELTA robot, which provides a stiff positioning functionality, the ACTIVE ANKLE provides a stiff orientating feature, due to the employment of parallel structures within the three kinematic chains.

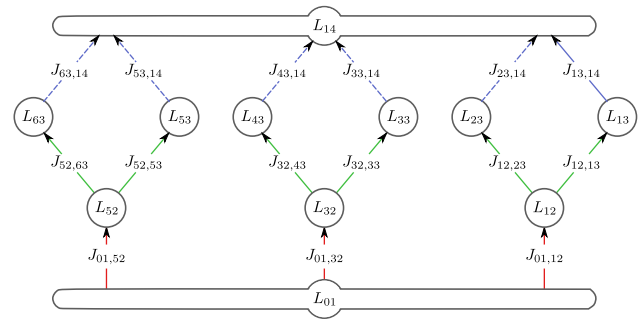


Fig. 3: Link graph of the parallel manipulator ACTIVE ANKLE, including $n = 11$ links and $m = 15$ joints.

2.2 Design and Construction

The mechanical layout of ACTIVE ANKLE is modular and depicted in Figure 2: the device features three rotative actuators fixed to the base. Each of the three motors drives a spatial quadrilateral consisting of a symmetric crank, two rods, and a line segment on the mobile platform. The three line segments mutually intersect orthogonally and together form a spatial cross on the end-effector link. The total weight of the mechanism including the three actuators is 1.8 Kg. With regard to the electronics, the device features three actuator modules which include a brushless DC motor coupled with harmonic gear drives (nominal torque 28 N m, weight 0.392 Kg), FPGA based control, and power electronics. Each actuator module is capable of a cascaded position, velocity, and current based torque control [35]. The presented prototype of this mechanism is designed to carry loads up to 30 Kg.

2.3 Topology and General Mobility

The topology of the mechanism is equivalent to DELTA robot as depicted in Figure 3. The $n = 11$ links L_i are enumerated as L_{01} , L_{12} , L_{13} , L_{14} , L_{23} , L_{32} , L_{33} , L_{43} , L_{52} , L_{53} , and L_{63} . The $m = 15$ joints $J_{i,j}$ are distinguished using double indices, as indicated in Figure 3. The number of independent loops of the ACTIVE ANKLE is computed with $c = m - n + 1 = 15 - 11 + 1 = 5$. For computing the general mobility number by means of the Kutzbach-Grübler formula

$$d_s(\mathcal{M}) = s \cdot (n - m - 1) + f = s \cdot (-c) + f,$$

the total number of freedoms $f = \sum_{ij} f_{ij}$ needs to be determined: three rotative joints, six spherical joints, and six universal joints, result in $f = 3 \cdot 1 + 6 \cdot 3 + 6 \cdot 2 = 3 + 18 + 12 = 33$, yielding a general mobility of

$$d_s(\mathcal{M}) = 6 \cdot (11 - 15 - 1) + 33 = 3.$$

Table 1: Overview of spatial parallel manipulators with general mobility d with distributions of degrees of freedom to k kinematic chains (legs), in accordance to [12].

	$d = 2$	$d = 3$	$d = 4$	$d = 5$	$d = 6$
$k = 2$					
$k = 3$	–				
$k = 4$	–	–			
$k = 5$	–	–	–		
$k = 6$	–	–	–	–	

Table 2: Examples of mechanisms with respect to type and mobility. *Watt’s and Chebyshev’s linkages are almost prismatic [19].

Mechanism type			General mobility d		
Name	Group	Dim.	1	3	6
Position	P^2	2	Peaucellier–Lipkin*	–	–
Flat	P^2R	3	Planar 4R	Planar Stewart	–
Spherical	R^3	3	Spherical 4R	Agile Eye, Argos	–
Position	P^3	3	Sarrus	Delta robot	–
Spatial	P^3R^3	6	Bennett 4R	Active Ankle	Stewart

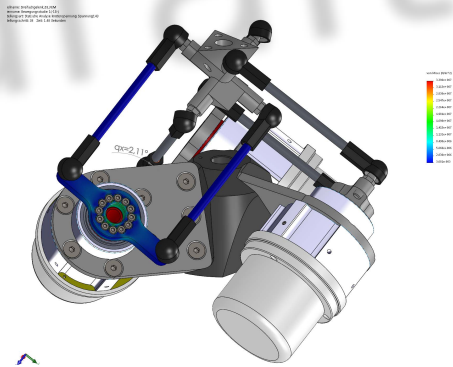


Fig. 4: FEM analysis of the ACTIVE ANKLE.

Since the device is *almost* spherical, the motion parameter s equals six (spatial) and not three (spherical).

2.4 Design Features

The mechanism’s homogeneous and simple design leads to a low link diversity, permits a low-cost construction, and provides robustness against production inaccura-

cies. A crucial feature of the mechanism’s design is the stress distribution among the structure. The six rods that transmit the forces from the cranks to the platform are only loaded with forces along their axes due to the spherical joints attached to them. Moreover, any force applied along the direction of its platform’s torsional axis can be supported without an active torque in the motors.

A multibody dynamics simulation analysis and a subsequent FEM analysis have been performed to check the deformation of the critical parts as rods and cranks under desired loads (Figure 4). A force corresponding to the weight of the exoskeleton is applied to the end effector and the forces in the spherical joints are measured. In the zero configuration, this force – equivalent to 350 N perpendicular to the end effector’s top plate – leads to a reaction force of approximately 100N in each spherical joint. The selected ball and socket joints are designed for a maximum axial tensile force of 600N in housing axis and a pivot angle of maximum of $\pm 25^\circ$. The same magnitude of force occurs in the rods and this force has been found to be less than the buckling force of the rods (i.e. 2120N). Thus, it is ensured that

Mechanism	Ref.	Links n	Joints m	Loops c
RRR / Cardan	[37]	4	3 (6)	0 (3)
Agile Eye / Wrist	[15]	8	9	2
AsySPM	[44]	11	13	3
CamSPM3	[40]	8	10	4
Hexasphere	[39]	14	19	6
Active Ankle	[34]	11	15	5

Table 3: A comparison of mechanisms, in terms of their members, links n , joints m , and number of independent loops $c = m - n + 1$; quoted from [35].

the mechanism resists from buckling in all possible configurations [35].

2.5 Design Comparison

In this section, the design of the almost-spherical mechanism Active Ankle is analyzed from a principal and from an application-motivated point of view: First, its design is compared to that of spherical mechanisms, and second, its design is set into contrast with devices intended to interoperate with the human ankle.

Spherical Mechanisms. In Table 3, the almost-spherical ACTIVE ANKLE is briefly compared to a set of (purely) spherical devices.³ The RRR chain and the Cardan mechanism [37] with three intersecting axes represent the most simple spherical devices: due to their serial construction, they lack the stiffness that is offered by their parallel counterparts. AGILE EYE and its variants are Spherical Parallel Manipulators (SPM) which offer high speeds for low payloads. Due to their design, they require high manufacturing and assembly accuracies. The design of the Asymmetrical Spherical Parallel Manipulator ASYSPM [44] involves the use of large number of different parts due to its asymmetrical leg configuration, . In comparison to the Active Ankle, the 3-SPS manipulator (CAMSPM3 in Table 3) [40] follows a complementary actuation approach: prismatic, instead of revolute joints are employed to actuate the platform. The HEXASPHERE [39] is a redundant SPM that features six motors to achieve the three rotative degrees of freedom of the platform.

Ankle Exoskeletons The ACTIVE ANKLE is priorly designed to work as an active interface to three degree-of-freedom (DOF) human joints. Its application at the

³ The presented comparison is an outline of a more detailed argumentation [35].

hip and the ankle joints within the novel full body RECUPERA exoskeleton [22] is presented in Section 5 (Figure 18). While the exoskeleton is primarily designed for upper body rehabilitation⁴, the main purpose of the legs is to transfer the load of the upper body exoskeleton system to the ground and provide some mobility features (e.g. sitting, standing, walking etc.) to the human subject: the RECUPERA legs and the integrated ACTIVE ANKLE instances are considered as *load transfer* devices according to the classification by Herr.⁵ In contrast to the similar load carrying exoskeleton BLEEX [46] which only features four active DOF per leg, the RECUPERA exoskeleton provides seven active DOF in each leg, due to the role of ACTIVE ANKLE as a modular spherical unit. The hydraulically-damped ankle-foot orthosis by Yamamoto et al. [45] and the knee-ankle-foot exoskeleton KAFO driven by artificial pneumatic muscles [32] both only provide a single DOF at the ankle joint of the human.

3 Inverse Kinematics

In this section, the points on the moving platform and crank circles are parameterized and kinematic constraint equations for this mechanism are derived. In Table 4, an overview of the nature of kinematics problems is presented based on the dimensionality of the input and output variables and the number of constraint equations. In particular, the inverse and rotative inverse kinematics problems are presented along with their solution methods.

The section is organized as follows: In Section 3.1, the mechanism’s architecture and its constraint equations are introduced, in Section 3.2 an analytical solution to the inverse kinematics problem is provided. Finally, Section 3.3 presents an efficient solution method to the rotative inverse kinematics problem which enables controlling the mechanism kinematically in the spherical task space.

⁴ The exoskeleton designs for upper body rehabilitation are usually attached to a fixed base (e.g. ARMIN [30], Recupera wheelchair system [25]) or to the patient’s torso (e.g. RUPERT[17]) which either reduces the mobility of patients or forces the patient to carry the weight of the exoskeleton which might be difficult for weaker stroke patients. A more detailed survey of exoskeletons for upper body rehabilitation can be found in [14]

⁵ Herr [16] distinguishes parallel-limb exoskeletons according to their function, ‘load transfer to the ground’, ‘torque and work augmentation’, and ‘increase human endurance’. Active devices are named ‘exoskeletons’, passive devices are named ‘orthoses’.

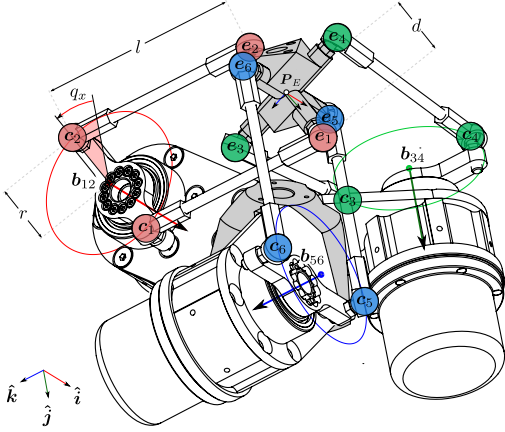


Fig. 5: A posture of the ACTIVE ANKLE corresponding to the configuration $\mathbf{q} = (q_x, q_y, q_z) \approx (-25^\circ, 0^\circ, 0^\circ)$. The design parameters are $d = r = 35$ mm and $l = 100$ mm.

3.1 Mechanism Architecture and Constraint Equations

The six points $(\mathbf{e}_1, \dots, \mathbf{e}_6)$ on the end effector lay on a sphere with radius d . The points \mathbf{c}_i and \mathbf{c}_j rotate around \mathbf{b}_{ij} in circles of radius r for $ij \in \{12, 34, 56\}$. The length of the six rods is denoted by l . The global frame O is coincident with the end effector position \mathbf{e} when the mechanism is in its zero-configuration (Figure 2). The unit vectors $\hat{\mathbf{s}}$, $\hat{\mathbf{n}}$ and $\hat{\mathbf{a}}$ are vectors along the x_E , y_E and z_E axes respectively expressed in the global frame O . In this section, the parameterizations of the end effector and crank points are presented and the constraint equations of the mechanism are derived.

End effector points The points \mathbf{e}_i , $i \in \{1, \dots, 6\}$ are rigidly attached to the end-effector. Figure 5 shows that the pair of points $(\mathbf{e}_1, \mathbf{e}_2)$ lies on a line $\mathcal{L}_{12} = (\mathbf{e}, \hat{\mathbf{n}})$ along unit vector $\hat{\mathbf{n}}$ passing through point \mathbf{e} . Similarly, the pairs $(\mathbf{e}_3, \mathbf{e}_4)$ and $(\mathbf{e}_5, \mathbf{e}_6)$ lie on lines $\mathcal{L}_{34} = (\mathbf{e}, \hat{\mathbf{a}})$ and $\mathcal{L}_{56} = (\mathbf{e}, \hat{\mathbf{s}})$ respectively. The coordinates of these points in terms of end effector position (\mathbf{e}) and orientation $(\hat{\mathbf{s}}, \hat{\mathbf{n}}, \hat{\mathbf{a}})$ are expressed as:

$$\begin{aligned} \mathbf{e}_1 &= \mathbf{e} + d \cdot \hat{\mathbf{n}} & \mathbf{e}_2 &= \mathbf{e} - d \cdot \hat{\mathbf{n}} \\ \mathbf{e}_3 &= \mathbf{e} + d \cdot \hat{\mathbf{a}} & \mathbf{e}_4 &= \mathbf{e} - d \cdot \hat{\mathbf{a}} \\ \mathbf{e}_5 &= \mathbf{e} + d \cdot \hat{\mathbf{s}} & \mathbf{e}_6 &= \mathbf{e} - d \cdot \hat{\mathbf{s}} \end{aligned} \quad (1)$$

The position vectors of six end effector points are stored column-wise in matrix $\mathbf{E} = (\mathbf{e}_1 \dots \mathbf{e}_6)$. The parameterization of six end effector points using the end effector pose is implemented in the method EPL (Alg. 2).

Crank points The crank points \mathbf{c}_i , $i \in \{1, \dots, 6\}$ are allowed to move on the circles defined by the motion of

three actuators. The pair of points $(\mathbf{c}_i, \mathbf{c}_j)$ lie diametrically opposite to each other on a circle of radius r with center \mathbf{b}_{ij} , $ij \in \{12, 34, 56\}$. The position vector of six crank points are parameterized using input joint angles (q_x, q_y, q_z) with the set of equations

$$\begin{aligned} \mathbf{c}_1(q_x) &= \mathbf{b}_{12} + \mathbf{c}_{12}(q_x) & \mathbf{c}_2(q_x) &= \mathbf{b}_{12} - \mathbf{c}_{12}(q_x) \\ \mathbf{c}_3(q_y) &= \mathbf{b}_{34} + \mathbf{c}_{34}(q_y) & \mathbf{c}_4(q_y) &= \mathbf{b}_{34} - \mathbf{c}_{34}(q_y) \\ \mathbf{c}_5(q_z) &= \mathbf{b}_{56} + \mathbf{c}_{56}(q_z) & \mathbf{c}_6(q_z) &= \mathbf{b}_{56} - \mathbf{c}_{56}(q_z) \end{aligned} \quad (2)$$

In (2), centers $(\mathbf{b}_{12}, \mathbf{b}_{34}, \mathbf{b}_{56})$ lie on (yz, zx, xy) planes at a distance of l units along (z, x, y) axes respectively. The general points $(\mathbf{c}_{12}, \mathbf{c}_{34}, \mathbf{c}_{56})$ on these circles are described as

$$\begin{aligned} \mathbf{b}_{12} &= l \cdot \hat{\mathbf{k}}, & \mathbf{c}_{12}(q_x) &= r \cdot \cos(q_x) \cdot \hat{\mathbf{j}} + r \cdot \sin(q_x) \cdot \hat{\mathbf{k}} \\ \mathbf{b}_{34} &= l \cdot \hat{\mathbf{i}}, & \mathbf{c}_{34}(q_y) &= r \cdot \cos(q_y) \cdot \hat{\mathbf{k}} + r \cdot \sin(q_y) \cdot \hat{\mathbf{i}} \\ \mathbf{b}_{56} &= l \cdot \hat{\mathbf{j}}, & \mathbf{c}_{56}(q_z) &= r \cdot \cos(q_z) \cdot \hat{\mathbf{i}} + r \cdot \sin(q_z) \cdot \hat{\mathbf{j}} \end{aligned}$$

The position vectors of six crank points are stored column-wise in matrix $\mathbf{C} = (\mathbf{c}_1 \dots \mathbf{c}_6)$. The parameterization of six crank points using the input joint angles is implemented in the method CPL (Alg. 3).

Kinematic constraint equations The length of the line segment joining the crank points (\mathbf{c}_i) to the end effector points (\mathbf{e}_i) equals the rod length l .

$$\|\mathbf{e}_i - \mathbf{c}_i\| = l, \quad i \in \{1, \dots, 6\} \quad (3)$$

Substituting (1) and (2) in (3), and squaring both sides, the six distance constraints equations are derived:

$$\begin{aligned} (e_x + d \cdot n_x)^2 + (e_y + d \cdot n_y - r \cdot \cos(q_x))^2 \\ + (e_z + d \cdot n_z - l - r \cdot \sin(q_x))^2 = l^2 \end{aligned} \quad (4)$$

$$\begin{aligned} (e_x - d \cdot n_x)^2 + (e_y - d \cdot n_y + r \cdot \cos(q_x))^2 \\ + (e_z - d \cdot n_z - l + r \cdot \sin(q_x))^2 = l^2 \end{aligned} \quad (5)$$

$$\begin{aligned} (e_x + d \cdot a_x - l - r \cdot \sin(q_y))^2 + (e_y + d \cdot a_y)^2 \\ + (e_z + d \cdot a_z - r \cdot \cos(q_y))^2 = l^2 \end{aligned} \quad (6)$$

$$\begin{aligned} (e_x - d \cdot a_x - l + r \cdot \sin(q_y))^2 + (e_y - d \cdot a_y)^2 \\ + (e_z - d \cdot a_z + r \cdot \cos(q_y))^2 = l^2 \end{aligned} \quad (7)$$

$$\begin{aligned} (e_x + d \cdot s_x - r \cdot \cos(q_z))^2 + (e_y + d \cdot s_y - l \\ - r \cdot \sin(q_z))^2 + (e_z + d \cdot s_z)^2 = l^2 \end{aligned} \quad (8)$$

$$\begin{aligned} (e_x - d \cdot s_x + r \cdot \cos(q_z))^2 + (e_y - d \cdot s_y - l \\ + r \cdot \sin(q_z))^2 + (e_z - d \cdot s_z)^2 = l^2 \end{aligned} \quad (9)$$

Type	Well-determined					Over-determined				
	Name	In	Eqs	Out	Method	Name	In	Eqs	Out	Method
Inverse	RIKP	\mathbf{R}_E	$\xrightarrow{6}$	(\mathbf{q}, \mathbf{e})	(Alg. 6)	IKP	$(\mathbf{R}_E, \mathbf{e})$	$\xrightarrow{6}$	\mathbf{q}	(Alg. 1)
	IKP*	$(\mathbf{R}_E, \mathbf{e})$	$\xrightarrow{3}$	\mathbf{q}	(Alg. 4)					
Forward	FKP	\mathbf{q}	$\xrightarrow{6}$	$(\mathbf{R}_E, \mathbf{e})$	(Alg. 7)	TFKP	$(\mathbf{q}, \mathbf{R}_E)$	$\xrightarrow{6}$	\mathbf{e}	–
	TFKP*	$(\mathbf{q}, \mathbf{R}_E)$	$\xrightarrow{3}$	\mathbf{e}	(Alg. 5)					

Table 4: Overview of problem characteristics, $\dim(\mathbf{R}_E) = 3$, $\dim(\mathbf{e}) = 3$, $\dim(\mathbf{q}) = 3$

3.2 Inverse Kinematics

Problem 1 (Inverse Kinematics) The Inverse Kinematics Problem (IKP) is defined as the problem of finding the input joint angles needed to achieve a specific pose of the end effector [21], formally,

$$[q_x, q_y, q_z] = \text{IKP}(\mathbf{P}_E), \quad \mathbf{P}_E \in SE(3),$$

where \mathbf{P}_E is the homogeneous transformation matrix of the end effector E with respect to the global frame O and $[q_x, q_y, q_z]$ are the active rotative joint angles.

$$\mathbf{P}_E = \begin{bmatrix} s_x & n_x & a_x & e_x \\ s_y & n_y & a_y & e_y \\ s_z & n_z & a_z & e_z \\ 0 & 0 & 0 & 1 \end{bmatrix}$$

It must be noted that the system of non-linear equations is overdetermined in context of the IKP as the number of unknowns (three) is less than the number of equations (six).

The method IKM in Alg. 1 provides an analytical solution method to IKP. The computation of the intersections of sphere and circle in Line 4 and Line 5 of Alg. 1 can be conducted by means of the intersection method SPHINT (Alg. 9) for three spheres.⁶ In Line 7, a pair of antipodal points is selected from the set of four intersection points by maximizing the cosine similarity between two normalized difference vectors. The line segment between the selected two points represents the current alignment of the rod. The angle between the current alignment and the zero reference alignment (Line 9) of one rod yields the angle of one input joint, determined in Line 10 of Alg. 1.

Since the IKM solution depends on the knowledge of the end effector shift (e_x, e_y, e_z) , it is not sufficient for achieving a kinematic control of the mechanism in spherical task space $SO(3)$. Therefore it is required to

⁶ For a given a circle $\mathcal{C}(\mathbf{m}_C, r_C, \hat{\mathbf{n}}_C)$ with midpoint \mathbf{m}_C , radius r_C , and unit normal $\hat{\mathbf{n}}_C$, two substituting spheres $\mathcal{S}_A(\mathbf{m}_A, r_A)$ and $\mathcal{S}_B(\mathbf{m}_B, r_B)$ are given by the midpoints $\mathbf{m}_A, \mathbf{m}_B = \mathbf{m}_C \pm \frac{4}{3} \cdot r_C \cdot \hat{\mathbf{n}}_C$ and the radii $r_A = r_B = \frac{5}{3} \cdot r_C$.

calculate the input joint angles only from the desired orientation of the end effector.

3.3 Rotative Inverse Kinematic Model

Problem 2 (Rotative Inverse Kinematics) The Rotative Inverse Kinematic Problem (RIKP) is to find the input joint angles needed to achieve a desired orientation of the end effector without having the knowledge of end effector position, formally,

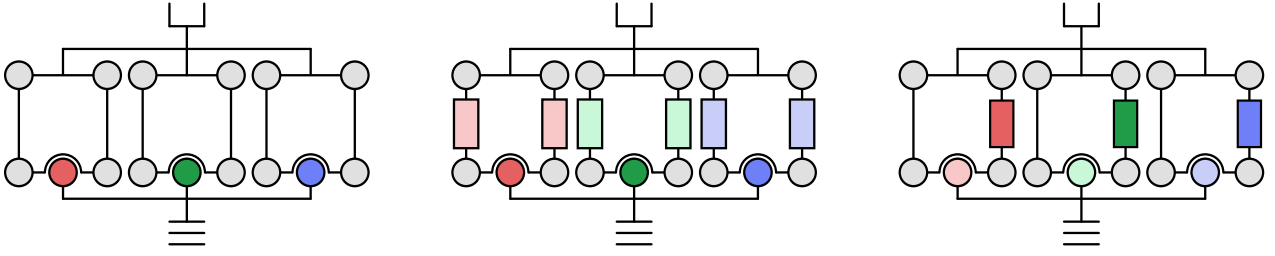
$$[q_x, q_y, q_z, e_x, e_y, e_z] = \text{RIKP}(\mathbf{R}_E), \quad \mathbf{R}_E \in SO(3),$$

where, \mathbf{R}_E is the rotation matrix of the end effector w.r.t the global frame, $[q_x, q_y, q_z]$ and $[e_x, e_y, e_z]$ are the active rotative joint angles and end effector shift respectively.

In this case, the system of nonlinear equations (4–9) is well determined as the number of unknowns is equal to the number of equations. To the best knowledge of the authors, it is not possible to derive a closed form solution to this problem due to coupled nature of the constraint equations. Instead of employing standard nonlinear solvers, a novel tailored and efficient algorithm is presented which is suitable for real time control of this mechanism. Its core idea is to decompose the overall equation system into two different equation sets and orthogonally iterate between their solutions to achieve the required overall solution with a desired accuracy. For concrete explanation, two subproblems related to the geometry of ACTIVE ANKLE are presented, namely, the Relaxed Inverse Kinematic Problem (IKP*) and the Relaxed Translative Forward Kinematic Problem (TFKP*). Based on their analytical solutions, the solution to the rotative inverse kinematic problem is presented.

3.3.1 Relaxed Inverse Kinematic Model

Since the nature of inverse kinematic problem is overdetermined (see Table 4), the two rod equations in each



(a) Physical setup of the ACTIVE ANKLE. (b) Relaxed structure for IKM* (Alg. 4). (c) Relaxed structure for TFKM* (Alg. 5).

Fig. 6: The mechanism ACTIVE ANKLE and relaxed variants featuring additional freedoms (virtual joints).

Algorithm 1 Inverse kinematic model (IKM)

Require: Target pose \mathbf{P}_e
Ensure: Joint configuration (q_x, q_y, q_z)

- 1: **function** IKM(\mathbf{P}_e)
- 2: $(\mathbf{e}_1, \dots, \mathbf{e}_6) \leftarrow \text{EPL}(\mathbf{P}_e)$ ▷ Platform coords
- 3: **for** $ij \in \{12, 34, 56\}$ **do**
- 4: $\mathbf{p}_{i+}, \mathbf{p}_{i-} \leftarrow \mathcal{S}(\mathbf{e}_i, d_i) \cap \mathcal{C}(\mathbf{b}_{ij}, \frac{c}{2}, \hat{\mathbf{z}}_{ij})$
- 5: $\mathbf{p}_{j+}, \mathbf{p}_{j-} \leftarrow \mathcal{S}(\mathbf{e}_j, d_j) \cap \mathcal{C}(\mathbf{b}_{ij}, \frac{c}{2}, \hat{\mathbf{z}}_{ij})$
 ▷ Sphere-circle intersections for i and j
- 6: $\mathcal{I} \leftarrow \{\mathbf{p}_{i+}, \mathbf{p}_{i-}\}, \mathcal{J} \leftarrow \{\mathbf{p}_{j+}, \mathbf{p}_{j-}\}$
- 7: $\mathbf{p}_+, \mathbf{p}_- \leftarrow \underset{\mathbf{p}_i \in \mathcal{I}, \mathbf{p}_j \in \mathcal{J}}{\text{argmax}} ((\mathbf{p}_i - \mathbf{b}_{ij})^\circ * (\mathbf{b}_{ij} - \mathbf{p}_j)^\circ)$
- 8: $\mathbf{r}_{ij} \leftarrow \mathbf{p}_+ - \mathbf{p}_-$ ▷ Antipodes
- 9: $\mathbf{d}_{ij} \leftarrow \mathbf{c}_i^{(0)} - \mathbf{c}_j^{(0)}$ ▷ Zero Posture
- 10: $q_x, q_y, q_z \leftarrow \angle(\mathbf{d}_{12}, \mathbf{r}_{12}), \angle(\mathbf{d}_{34}, \mathbf{r}_{34}), \angle(\mathbf{d}_{56}, \mathbf{r}_{56})$
- 11: **return** (q_x, q_y, q_z)

leg are subtracted to obtain a well determined system of leg equations. Problem 1 is relaxed in the sense that it ensures $l_{e_1 c_1} = l_{e_2 c_2}, l_{e_3 c_3} = l_{e_4 c_4}, l_{e_5 c_5} = l_{e_6 c_6}$ and not $l_{e_i c_i} = l, i \in \{1, \dots, 6\}$. A geometric interpretation of this relaxation is shown in Figure 6b: the rods can be interpreted as virtual prismatic joints which change their lengths in pair in each leg.

Three leg equations Subtracting (5) from (4), (7) from (6), (9) from (8), the three leg equations are derived.

$$\begin{aligned} r e_y \cos q_x + r(e_z - l) \sin q_x + d(ln_z - \mathbf{e} * \mathbf{n}) &= 0 \\ r e_z \cos q_y + r(e_x - l) \sin q_y + d(la_x - \mathbf{e} * \mathbf{a}) &= 0 \\ r e_x \cos q_z + r(e_y - l) \sin q_z + d(ls_y - \mathbf{e} * \mathbf{s}) &= 0 \end{aligned} \quad (10)$$

The three leg equations, with the leg index $j \in \{1, 2, 3\}$, are of the form:

$$E_j \cdot \cos(q_j) + F_j \cdot \sin(q_j) + G_j = 0 \quad (11)$$

Relaxed IKP Solution Using the tangent half angle substitution,

$$t_j = \tan\left(\frac{q_j}{2}\right), \quad \cos(q_j) = \frac{1 - t_j^2}{1 + t_j^2}, \quad \sin(q_j) = \frac{2t_j}{1 + t_j^2},$$

a quadratic equation in t is obtained

$$(G_j - E_j) \cdot t_j^2 + 2 \cdot F_j \cdot t_j + (G_j + E_j) = 0. \quad (12)$$

The two solutions of the above quadratic equation is given by:

$$t_{j1,2} = \frac{-F_j \pm \sqrt{E_j^2 + F_j^2 - G_j^2}}{G_j - E_j} \quad (13)$$

$$q_{j+}, q_{j-} = 2 \cdot \text{atan2}(-F_j \pm H_j, G_j - E_j)$$

where $H_j = \sqrt{E_j^2 + F_j^2 - G_j^2}$. The expressions for E_j , F_j and G_j for the three legs are given in Table 5.

The absolute minimum of the two solutions is chosen so that the mechanism stays close to the zero configuration and respects the physical constraints imposed by either link intersection or limits of passive spherical joints. The solution is implemented in the method IKM* in Alg. 4.

3.3.2 Relaxed Translative Forward Kinematic Model

Translative Forward Kinematic Problem (TFKP) is defined as the problem of finding the end effector shift from the input joint configuration and desired orientation of the end effector, formally,

$$\mathbf{e} = \text{TFKP}(q_x, q_y, q_z, \mathbf{R}_E). \quad (14)$$

Table 5: Parameters for IKM* solution

Leg Index (j)	E_j	F_j	G_j
$j = 1$	$r e_y$	$r(e_z - l)$	$d(ln_z - \mathbf{e} * \mathbf{n})$
$j = 2$	$r e_z$	$r(e_x - l)$	$d(la_x - \mathbf{e} * \mathbf{a})$
$j = 3$	$r e_x$	$r(e_y - l)$	$d(ls_y - \mathbf{e} * \mathbf{s})$

Algorithm 2 Calculation of effector points (EPL)**Require:** Homogeneous transformation of end effector \mathbf{P}_E **Ensure:** End effector point matrix \mathbf{E}

```

1: function EPL( $\mathbf{P}_E$ )
2:    $\begin{bmatrix} \hat{\mathbf{s}} & \hat{\mathbf{n}} & \hat{\mathbf{a}} & \mathbf{e} \\ 0 & 0 & 0 & 1 \end{bmatrix} \leftarrow \mathbf{P}_E$  ▷ Extraction
3:    $\mathbf{e}_1 \leftarrow \mathbf{e} + d \cdot \hat{\mathbf{n}}, \quad \mathbf{e}_2 \leftarrow \mathbf{e} - d \cdot \hat{\mathbf{n}}$ 
4:    $\mathbf{e}_3 \leftarrow \mathbf{e} + d \cdot \hat{\mathbf{a}}, \quad \mathbf{e}_4 \leftarrow \mathbf{e} - d \cdot \hat{\mathbf{a}}$ 
5:    $\mathbf{e}_5 \leftarrow \mathbf{e} + d \cdot \hat{\mathbf{s}}, \quad \mathbf{e}_6 \leftarrow \mathbf{e} - d \cdot \hat{\mathbf{s}}$ 
6:    $\mathbf{E} \leftarrow (\mathbf{e}_i : 1 \leq i \leq 6)$ 
7:   return  $\mathbf{E}$ 

```

The solution to this problem provides the parasitic motion of the end effector. As noted in Table 4, this problem is an over-determined problem as the number of unknowns are three while the number of constraint equations equals to six. Each rod length constraint (4–9) represents the equation of a sphere where the end effector point $[e_x, e_y, e_z]$ moves on its surface. They represent the system of equations of six spheres and the end effector of ACTIVE ANKLE must lie at their intersection point. However, while solving the IKM* it is already ensured that the two rod lengths forming a leg should be the same. So, end effector coordinates can be computed by solving the three rod equations including one from each leg which makes the problem well-determined. The problem is relaxed in the sense that it ensures either $l_{e_1c_1} = l_{e_3c_3} = l_{e_5c_5} = l$ or $l_{e_2c_2} = l_{e_4c_4} = l_{e_6c_6} = l$ and not $l_{e_i c_i} = l, i \in \{1, \dots, 6\}$. A geometric interpretation of this relaxation is shown in Figure 6c: the unchosen rods can be interpreted as virtual prismatic joints which will adjust their lengths so that the chosen rod length becomes equal to l after solving the problem. Overall, the six sphere intersection problem reduces to a three sphere intersection problem.

Relaxed TFKP Solution. Three spheres intersect in maximally two points [38]. Without the loss of generality, one can choose to solve for spheres represented by (4), (6) and (8). This particular choice of sphere centers (\mathbf{s}_i) and radii $r_i, i \in \{1, 2, 3\}$ is shown in the method TFKM* in Alg. 5. The end-effector coordinates are estimated using

$$\mathbf{e}_+, \mathbf{e}_- = \text{SPHINT}(\mathbf{s}_1, \mathbf{s}_2, \mathbf{s}_3, r_1, r_2, r_3). \quad (15)$$

The method SPHINT is specified in Alg. 9 in Appendix B. The solution with a norm less than equal to d is selected to avoid the mechanism to leave its assembly. This is implemented in the method TFKM* in Alg. 5.

Algorithm 3 Calculation of crank points (CPL)**Require:** Input joint angles $[q_x, q_y, q_z]$ **Ensure:** Crank point matrix \mathbf{C}

```

1: function CPL( $q_x, q_y, q_z$ )
2:    $\mathbf{c}_1 \leftarrow (0, r \cdot \cos q_x, l + r \cdot \sin q_x)^T$ 
3:    $\mathbf{c}_2 \leftarrow (0, -r \cdot \cos q_x, l - r \cdot \sin q_x)^T$ 
4:    $\mathbf{c}_3 \leftarrow (l + r \cdot \sin q_y, 0, r \cdot \cos q_y)^T$ 
5:    $\mathbf{c}_4 \leftarrow (l - r \cdot \sin q_y, 0, -r \cdot \cos q_y)^T$ 
6:    $\mathbf{c}_5 \leftarrow (r \cdot \cos q_z, l + r \cdot \sin q_z, 0)^T$ 
7:    $\mathbf{c}_6 \leftarrow (-r \cdot \cos q_z, l - r \cdot \sin q_z, 0)^T$ 
8:    $\mathbf{C} \leftarrow (\mathbf{c}_i : 1 \leq i \leq 6)$ 
9:   return  $\mathbf{C}$ 

```

3.3.3 Solution Approach

The estimated end effector coordinates are defined as $\tilde{\mathbf{e}} = [\tilde{e}_x, \tilde{e}_y, \tilde{e}_z]$. In the sequel, the approximate nature of a variable x is expressed by using a tilde \tilde{x} . The homogeneous transformation matrix of the end effector w.r.t. the global frame is given by

$$\tilde{\mathbf{P}}_E = \begin{bmatrix} \mathbf{R}_E & \tilde{\mathbf{e}}_{3 \times 1} \\ \mathbf{0}_{1 \times 3} & 1 \end{bmatrix}. \quad (16)$$

With an estimated homogeneous transformation matrix ($\tilde{\mathbf{P}}_E$), the estimated positions of the six end effector points stored in matrix $\tilde{\mathbf{E}}$ are calculated with the help of Alg. 2 as

$$\tilde{\mathbf{E}} = \text{EPL}(\tilde{\mathbf{P}}_E). \quad (17)$$

The IKM* solution as presented in Section 3.3.1 is used to calculate the estimated input joint angles $\tilde{\mathbf{q}} = [\tilde{q}_x, \tilde{q}_y, \tilde{q}_z]$ required to achieve the estimated end effector position and desired orientation. It must be recalled that for the derivation of three leg equations (10), the two distance constraint equations of each rod constituting a leg are subtracted from each other and hence forcing the two virtual rod lengths of each leg to be equal. Thus, any approximate solution to the inverse kinematic model comes at a cost of incorrect leg lengths.

$$[\tilde{q}_x, \tilde{q}_y, \tilde{q}_z] = \text{IKM}^*(\tilde{\mathbf{P}}_E) \quad (18)$$

The estimated input joint angles are now used to estimate the position of six crank points using Alg. 3.

$$\tilde{\mathbf{C}} = \text{CPL}(\tilde{q}_x, \tilde{q}_y, \tilde{q}_z) \quad (19)$$

The estimated position vectors of the six end effector points ($\tilde{\mathbf{e}}_i$) and the six crank points ($\tilde{\mathbf{c}}_i$) are extracted from end effector points matrix $\tilde{\mathbf{E}}$ (17) and crank points matrix $\tilde{\mathbf{C}}$ (19) respectively. The length of six virtual rods are calculated from $\tilde{\mathbf{e}}_i$ and $\tilde{\mathbf{c}}_i$ using:

$$\|\tilde{\mathbf{e}}_i - \tilde{\mathbf{c}}_i\| = \tilde{l}_i, \quad i \in \{1, \dots, 6\} \quad (20)$$

Algorithm 4 Relaxed inverse kinematic model (IKM^{*})**Require:** Homogeneous transformation of end effector \mathbf{P}_E **Ensure:** Input joint angles $[q_x, q_y, q_z]$

```

1: function IKM*( $\mathbf{P}_E$ )
2:   for  $j \in (1, 2, 3)$  do
3:      $H_j \leftarrow \sqrt{E_j^2 + F_j^2 - G_j^2}$  ▷ Table 5
4:      $q_{j+}, q_{j-} \leftarrow 2 \cdot \text{atan2}(-F_j \pm H_j, G_j - E_j)$ 
5:      $q_{j+} \leftarrow \text{atan2}(\sin q_{j+}, \cos q_{j+})$  ▷ Wrap to  $\pm\pi$ 
6:      $q_{j-} \leftarrow \text{atan2}(\sin q_{j-}, \cos q_{j-})$  ▷ Wrap to  $\pm\pi$ 
7:      $q_j \leftarrow \min(|q_{j+}|, |q_{j-}|)$ 
8:    $[q_x, q_y, q_z] \leftarrow (q_j : 1 \leq j \leq 3)$ 
9:   return  $[q_x, q_y, q_z]$ 

```

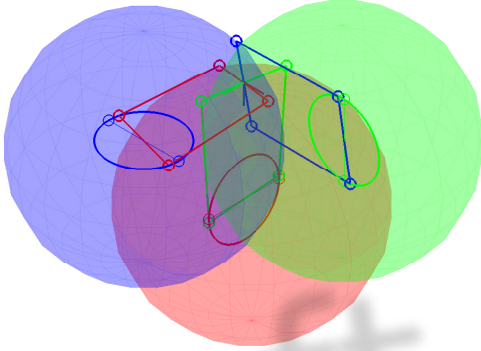


Fig. 7: Normal working mode, active joint angles: $(q_x, q_y, q_z) \approx (0.0872, 0.1748, 0.2614)$ and end effector shift: $(e_x, e_y, e_z) \approx (0.0127, 0.1515, 0.3807)$

A least square error function to minimize the change in virtual rod lengths is defined as follows:⁷

$$E_{\text{rgd}}(\tilde{\mathbf{e}}_i, \tilde{\mathbf{c}}_i) = \sum_{i=1}^6 (\tilde{l}_i - l)^2 \quad (21)$$

To minimize the least squared error, the new end effector coordinates ($\tilde{\mathbf{e}} = [\tilde{e}_x, \tilde{e}_y, \tilde{e}_z]$) are estimated. Solving for the new end effector position in each iteration is equivalent to solving the relaxed forward kinematic model in translative domain (see Section 3.3.2). The solution ensures that the leg lengths become equal to l .

$$\tilde{\mathbf{e}} = \text{TFKM}^*(\tilde{q}_x, \tilde{q}_y, \tilde{q}_z, \mathbf{R}_E) \quad (22)$$

The two solutions in TFKM^{*} lead to two distinct solutions for the RIKM, out of which we are primarily inter-

⁷ For improving computational efficiency, the error function can also be chosen to minimize the change in three instead of six rod lengths: the solution of IKM^{*} already ensures that the two rod lengths equal in each leg.

Algorithm 5 Relaxed translative forward kinematic model (TFKM^{*})**Require:** Input joint angles $[q_x, q_y, q_z]$ and rotation matrix \mathbf{R}_E **Ensure:** End effector position \mathbf{e}

```

1: function TFKM*( $q_x, q_y, q_z, \mathbf{R}_E$ )
2:    $(r_1, r_2, r_3) \leftarrow l$ 
3:    $\mathbf{s}_1 \leftarrow (-dn_x, r \cdot \cos q_x - dn_y, l - dn_z + r \cdot \sin q_x)^T$ 
4:    $\mathbf{s}_2 \leftarrow (l - da_x + r \cdot \sin q_y, -da_y, r \cdot \cos q_y - da_z)^T$ 
5:    $\mathbf{s}_3 \leftarrow (r \cdot \cos q_z - ds_x, l - ds_y + r \cdot \sin q_z, -ds_z)^T$ 
6:    $\mathbf{e}_+, \mathbf{e}_- \leftarrow \text{SPHINT}(\mathbf{s}_1, \mathbf{s}_2, \mathbf{s}_3, r_1, r_2, r_3)$  ▷ Alg. 9
7:   if  $\|\mathbf{e}_+\| < d$  then
8:      $\mathbf{e} \leftarrow \mathbf{e}_+$ 
9:   else
10:     $\mathbf{e} \leftarrow \mathbf{e}_-$ 
11:   return  $\mathbf{e}$ 

```

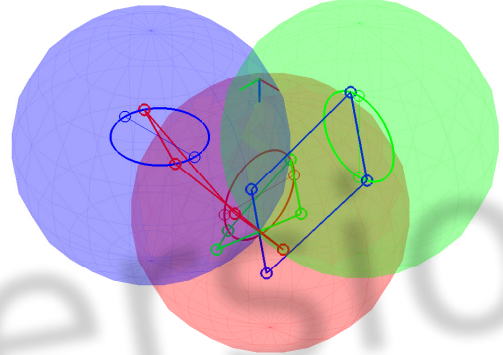


Fig. 8: Upside – down working mode, active joint angles: $(q_x, q_y, q_z) \approx (0.4566, 0.2377, 0.4663)$ and end effector shift: $(e_x, e_y, e_z) \approx (65.6274, 65.9876, 66.7599)$

ested in the solution with norm less than d . Each estimation of the end effector position using the method TFKM^{*} minimizes the least squared error function in the next iteration. Hence, the estimated end effector coordinates are substituted back into the (16) and the subsequent calculations are iterated until the $E_{\text{rgd}}(\tilde{\mathbf{e}}_i, \tilde{\mathbf{c}}_i) < \epsilon$ is achieved. The overall rotative inverse kinematic model is implemented in the method RIKM (Alg. 6). It must be noted that $\tilde{\mathbf{e}}$ is initialized as $\mathbf{0}$ at the beginning of the algorithm (Line 2) but this choice does not affect the convergence of the algorithm.⁸ The two almost spherical working modes (solutions to the RIKM) for an axis $\mathbf{u} \approx (0.2127, 0.5344, 0.8180)^T$ and angle $\phi \approx 0.3140$ are shown in Figure 7 and Figure 8. The numerical convergence towards normal working mode is depicted in Table 6.

⁸ Instead the convergence to the correct physical configuration is guaranteed by selecting the appropriate intersection point within TFKM^{*}.

Iteration	0	1	2
q_x	0.0872	0.0872	0.0872
q_y	0.1745	0.1748	0.1748
q_z	0.2612	0.2613	0.2614
e_x	0.0	0.0071	0.0127
e_y	0.0	0.1499	0.1515
e_z	0.0	0.3678	0.3807
E_{rgd}	0.3370	$4.12 \cdot 10^{-04}$	$4.29 \cdot 10^{-07}$

Table 6: A numerical example showing the convergence of RIKM for an axis $\mathbf{u} \approx (0.2127, 0.5344, 0.8180)^T$ and an angle $\phi \approx 0.3140$.

Algorithm 6 Rotative inverse kinematic model (RIKM)

Require: Desired orientation of the end effector, \mathbf{R}_E
Ensure: Joint angles $[q_x, q_y, q_z]$ and end effector shift $[e_x, e_y, e_z]$

```

1: function RIKM( $\mathbf{R}_E, \epsilon$ )
2:    $\tilde{\mathbf{P}}_E \leftarrow \begin{bmatrix} \mathbf{R}_E & \mathbf{0}_{3 \times 1} \\ \mathbf{0}_{1 \times 3} & 1 \end{bmatrix}$  ▷ Initialization
3:   while  $E_{\text{rgd}} < \epsilon$  do
4:      $(\tilde{\mathbf{e}}_1 \dots \tilde{\mathbf{e}}_6) \leftarrow \text{EPL}(\tilde{\mathbf{P}}_E)$  ▷ Alg. 2
5:      $(\tilde{q}_x, \tilde{q}_y, \tilde{q}_z) \leftarrow \text{IKM}^*(\tilde{\mathbf{P}}_E)$  ▷ Alg. 4
6:      $(\tilde{\mathbf{c}}_1 \dots \tilde{\mathbf{c}}_6) \leftarrow \text{CPL}(\tilde{q}_x, \tilde{q}_y, \tilde{q}_z)$  ▷ Alg. 3
7:      $E_{\text{rgd}} \leftarrow \sum_i^6 (||\tilde{\mathbf{e}}_i - \tilde{\mathbf{c}}_i|| - l)^2$  ▷ Rigidity error
8:      $\tilde{\mathbf{e}} \leftarrow \text{TFKM}^*(\tilde{q}_x, \tilde{q}_y, \tilde{q}_z, \mathbf{R}_E)$  ▷ Alg. 5
9:      $\tilde{\mathbf{P}}_E \leftarrow \begin{bmatrix} \mathbf{R}_E & \tilde{\mathbf{e}}_{3 \times 1} \\ \mathbf{0}_{1 \times 3} & 1 \end{bmatrix}$  ▷ Update
10:     $[q_x, q_y, q_z] \leftarrow [\tilde{q}_x, \tilde{q}_y, \tilde{q}_z]$ 
11:     $[e_x, e_y, e_z] \leftarrow [\tilde{e}_x, \tilde{e}_y, \tilde{e}_z]$ 
12:  return  $[q_x, q_y, q_z, e_x, e_y, e_z]$ 

```

Benchmarking and Convergence. The solution strategy presented above to solve RIKP is compared with some standard non-linear solvers like Levenberg-Marquardt (LM) and Trust Region Dog Leg (TRDL) implemented in fsolve function of MATLAB as well as constrained optimisation solver using Active Set algorithm implemented in MATLAB function called fmincon. A total of 1000 random orientation samples are chosen from the *physically* feasible workspace of the mechanism (Figure 14) and are provided as the input to this problem. RIKM solver demonstrates robust convergence inside the physically feasible workspace of the mechanism. The number of iterations for convergence and the CPU time⁹ of RIKM are recorded for benchmarking its efficiency in comparison to standard solvers for a tolerance of $\epsilon = 1.e^{-06}$ mm (See Figure 9 and Figure 10). With

⁹ Intel Core i7 CPU 950 @ 3.07GHz x 8PC, 6GB RAM

average iterations for convergence equals to 3.42 and CPU time equals to 2.58 milli-seconds, it was found that RIKM performed 21 times faster than TRDL based solver. Hence, it is the most suitable method to achieve a kinematic control on the ACTIVE ANKLE as described in Section 5.

Discussion. The computation scheme of the novel RIKM algorithm – that solves the problem of coupled motion kinematics in context of the ACTIVE ANKLE efficiently – is displayed in diagram in Figure 11. From that scheme, it can be observed that the auxiliary variables $\tilde{\mathbf{l}}$ – that reflect violations of structural (rigidity) constraints – can be interpreted as virtual joints. The method RIKM ensures that at termination after a few iterations (see Table 6), the values of $\tilde{\mathbf{l}}$ equal zero. From the viewpoint of kinematic synthesis, this consideration opens a perspective for extending the ACTIVE ANKLE from an almost spherical design to a fully-controllable six-DOF mechanism that, in particular, could also act as a perfect spherical mechanism (compare [27]).

4 Forward Kinematics

For reasoning about potential applications and future modifications of a novel mechanical design, its features and limitations require consideration. In particular, the workspace of a novel design needs to be characterized. Therefore, the forward kinematic problem of the ACTIVE ANKLE is firstly introduced together with a concise modeling as a numerical optimization problem in Section 4.1. Based on these prerequisites, the physical workspace of the ACTIVE ANKLE is evaluated in Section 4.2 with regard to the configuration space, the (primary) rotative taskspace, and the (secondary) translative taskspace. The analysis is focused on the physically realizable workspace that is constrained by the specific mode the mechanism is assembled in.¹⁰ In particular, the principal limitations (given by link intersection) of the physical taskspace are set into perspective with those given by the employed spherical joints. The rotative domain of the taskspace is visualized by means of rotation vectors (closely related to angle-axis representation and quaternions [5]). The color model has been adopted to represent the joint configuration of a certain posture.¹¹

¹⁰ A complementary analysis focusing on global aspects of ACTIVE ANKLE's workspace is available in [24].

¹¹ A bright red, green, or blue tone indicates a strong influence of particular joint (the x , y , or z -joint, respectively), compare Figure 12.

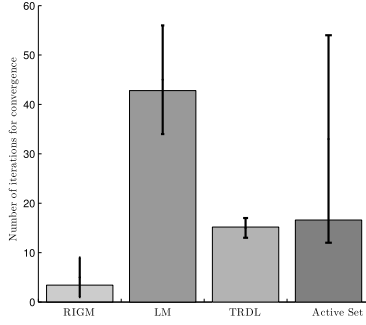


Fig. 9: Comparison of number of iterations for convergence amongst different RIKM solution strategies

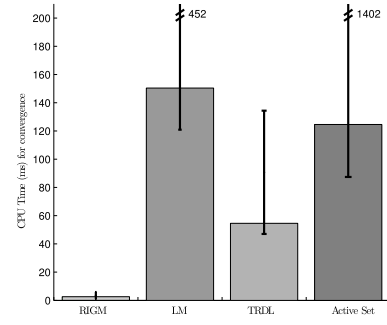


Fig. 10: Comparison of CPU time for convergence amongst different RIKM solution strategies

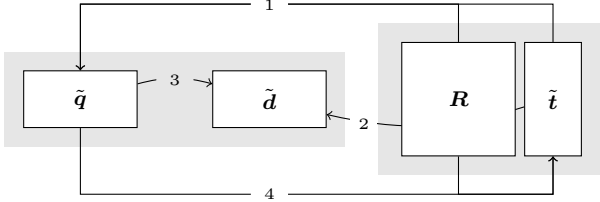


Fig. 11: Computation scheme of the rotative inverse method RIKM. The matrix of workspace variables is the end-effector pose $\tilde{\mathbf{P}}_E \cong (\mathbf{R}, \tilde{\mathbf{t}})$. The vector of configuration variables $\tilde{\mathbf{q}}$ is given by (q_x, q_y, q_z) . The vector of design variables, denoted by $\tilde{\mathbf{d}}$, includes the vector $\tilde{\mathbf{l}}$ that is checked for constraint violation in the abortion criterion of RIKM in Alg. 6. The computation in RIKM consists of the steps (1) IKM*, (2) EPL, (3) CPL, and (4) TFKM*.

4.1 Solution Approach

Problem 3 (Forward Kinematics) The forward kinematic problem (FKP) of the ACTIVE ANKLE is to compute a pose of the end effector \mathbf{P}_E for given joint angles (q_x, q_y, q_z) , as

$$\mathbf{P}_E = \text{FKP}(q_x, q_y, q_z). \quad (23)$$

While the inverse kinematic problem IKP (Prob. 1) is solved analytically (Section 3.2), the forward kinematics Prob. 3 is solved via a numerical optimization NFK($\mathbf{q}; \mathbf{P}_E^{(0)}$) in Alg. 7. The core of the numerical optimization is the formulation of a target function COST that, in essence, expresses the constraint violation between endeffector and base. With regard to this, the presented modeling and solution procedure is closely related to the approach described in [33]. Technically, the

computation of the function COST displayed in Alg. 8 relies on three summands explained next.

Distance summand (DS) The summand c reflects, as (3), the distance constraints given by the rod length l , as

$$c(\mathbf{E}, \mathbf{C}, l) = \sum_{i=1}^6 \left(\frac{\|\mathbf{e}_i - \mathbf{c}_i\|^2 - l^2}{l^2} \right)^2, \quad (24)$$

expressed by $\mathbf{E} = (\mathbf{e}_1 \dots \mathbf{e}_6)$ and $\mathbf{C} = (\mathbf{c}_1 \dots \mathbf{c}_6)$. Here, the points \mathbf{e}_i depend on the pose \mathbf{P}_E (EPL in Alg. 2) and the points \mathbf{c}_i depend on the configuration vector \mathbf{q} (CPL in Alg. 3).

Representation summands (RS) Instead of the matrix representation \mathbf{P}_E , the COST function is based on the vectorial representation of the end effector's pose

$$\mathbf{x} = (\phi, u_x, u_y, u_z, e_x, e_y, e_z)^T,$$

containing the angle-axis representation of orientation and three position variables. Due to the applied angle-axis representation, two technical cost summands are introduced for enforcing the algorithm to converge: the cost n , defined as

$$n(\mathbf{x}) = \left(\frac{\|(u_x, u_y, u_z)\|^2 - 1^2}{1^2} \right)^2. \quad (25)$$

represents a penalty for violation of the constraint $\|\hat{\mathbf{u}}\| = 1$. The third summand a , defined as

$$a(\mathbf{x}, \mathbf{s}) = \left(\frac{(\phi^2 + s_\phi^2) - \pi^2}{\pi^2} \right)^2, \quad (26)$$

represents a penalty for violation of the constraint $|\phi| \leq \pi$. Here, \mathbf{s} denotes the vector of slack variables $\mathbf{s} = (s_\phi)^T$ for modeling inequality constraints.

Algorithm 7 Numerical forward kinematics (NFK)

Require: Configuration $\mathbf{q} = (q_x, q_y, q_z)^T$, initial search pose $\mathbf{P}_E^{(0)}$

Ensure: An endeffector pose \mathbf{P}_E feasible for \mathbf{q}

- 1: **function** NFK($\mathbf{q}; \mathbf{P}_E^{(0)}$)
- 2: $\mathbf{C} \leftarrow \text{CPL}(\mathbf{q})$ ▷ Alg. 3
- 3: $\mathbf{x}^{(0)} \leftarrow \text{MAT2VEC}(\mathbf{P}_E^{(0)})$ ▷ Alg. 12
- 4: $\mathbf{s}^{(0)} \leftarrow \mathbf{0}$ ▷ Init. slacks
- 5: $\mathbf{x}^*, \mathbf{s}^* \leftarrow \underset{(\mathbf{x}, \mathbf{s})}{\text{argmin}} \text{COST}(\mathbf{x}^{(0)}, \mathbf{s}^{(0)}; \mathbf{C}, \mathbf{l})$ ▷ Optim.
- 6: $\mathbf{P}_E \leftarrow \text{VEC2MAT}(\mathbf{x}^*)$ ▷ Alg. 13
- 7: **return** \mathbf{P}_E

Algorithm 8 Vectorial constraint violation function

Require: Pose vector \mathbf{x} , slack vector \mathbf{s} , crank points \mathbf{C} , rod length l

Ensure: Scalar value v representing the constraint violation

- 1: **function** COST($\mathbf{x}, \mathbf{s}; \mathbf{C}, l$)
- 2: $\mathbf{P}_E \leftarrow \text{VEC2MAT}(\mathbf{x})$ ▷ Alg. 13
- 3: $\mathbf{E} \leftarrow \text{EPL}(\mathbf{P}_E)$ ▷ Alg. 2
- 4: $v \leftarrow c(\mathbf{E}, \mathbf{C}; l) + n(\mathbf{x}) + a(\mathbf{x}, \mathbf{s})$ ▷ (24, 25, 26)
- 5: **return** v

Method Based on the introduced cost terms, the numerical forward computation NFK in Alg. 7 is modeled as an quadratic unconstrained optimization method. For the initial pose $\mathbf{P}_E^{(0)}$ (Line 1) prior knowledge can be used or an initialization by the ‘zero’ or a ‘random’ pose is applied. For the optimization (Line 5) a standard gradient descent for local optimization, for example BFGS, can be applied. The conversion methods MAT2VEC and VEC2MAT are stated in Appendix C. Due to the non-negativity of the three summands of the target function COST, the function value

$$c(\mathbf{E}, \mathbf{C}, l) + n(\mathbf{x}) + a(\mathbf{x}, \mathbf{s}) = 0 \quad (27)$$

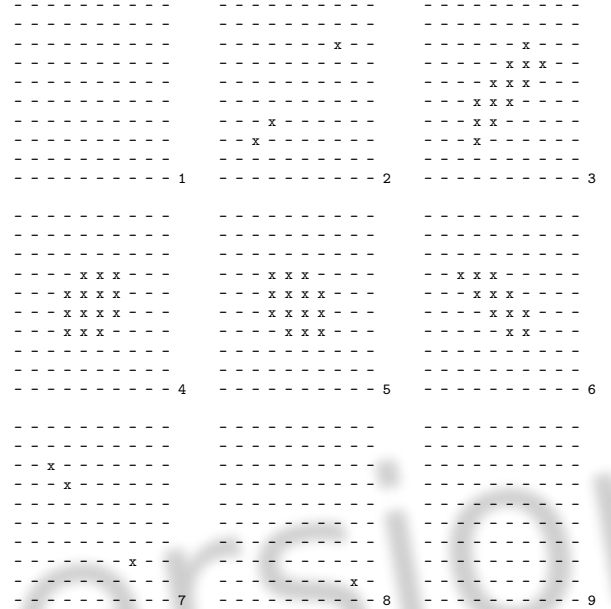
certifies an optimization result \mathbf{P}_E that fulfills all required constraints that are given in (24, 25, 26).

4.2 Workspace Characterization

In contrast to Prob. 3, that asks for the output poses of one joint configuration, the problem of workspace analysis is asking for the solvability of Prob. 3 for *all* poses $\mathbf{P}_E \in SE(3)$. As such, the analysis of workspace is crucial for the design and the operation of machines since it provides a ‘global view’ onto the properties of a mechanism.

Problem 4 (Workspace Analysis) Given the mechanism ACTIVE ANKLE, determine for each pose $\mathbf{P}_E \in$

Table 7: Layered illustration of the configuration domain of the ACTIVE ANKLE. The symbols ‘x’ and ‘-’ indicate the feasible and the infeasible joint angles $\mathbf{q} = (q_x, q_y, q_z) \in Q^3$ with $Q \approx (-69.2^\circ, -49.4^\circ, -29.6^\circ, -9.8^\circ, 9.8^\circ, 29.6^\circ, 49.4^\circ, 69.2^\circ, 89.0^\circ)$. For each of the nine arrays, $q_x \in Q$ is fixed while q_y and q_z vary.



$SE(3)$, if at least one joint configuration $\mathbf{q} = (q_x, q_y, q_z)^T$ exists such that the endeffector is located at \mathbf{P}_E . For each such \mathbf{q} , let the overall configuration be described as $(\mathbf{q}, \mathbf{P}_E, \mathbf{E}, \mathbf{C})$, so that the problem is formally be denoted as

$$\left\{ \mathbf{q}, \mathbf{P}_E, \mathbf{E}, \mathbf{C} \mid \text{FKP}(\mathbf{q}) = \mathbf{P}_E, \mathbf{E} = \text{EPL}(\mathbf{P}_E), \mathbf{C} = \text{CPL}(\mathbf{q}), \mathbf{P}_E \in SE(3) \right\}.$$

Since the input space has dimension three (\mathbf{q}), while the ambient dimension of the output space equals six (\mathbf{P}_E), the feasible output set of ACTIVE ANKLE is a lower dimensional.

In the remainder of this section, discrete approximations of the workspace of the ACTIVE ANKLE are provided by evaluating the forward geometry on regular grids in the configuration space. Instead of considering the overall vector $(\mathbf{q}, \mathbf{P}_E, \mathbf{E}, \mathbf{C})$ of Prob. 4 with $3 + 16 + 18 + 18 = 55$ variables, projections [4] to the essential (1) *configuration*, (2) *translative*, and (3) *rotative* domains are explored. Three further constraints are introduced in the sequel to judge the physical realizability of obtained configurations.

Simplex constraints (SC) Let $\Delta(\mathbf{a}, \mathbf{b}, \mathbf{c}, \mathbf{d})$ denote the 3-simplex spanned by four vertices $\mathbf{a}, \mathbf{b}, \mathbf{c}, \mathbf{d}$ and let

$\text{svol}(\Delta)$ denote its *signed volume*, computed as

$$\text{svol}(\Delta(\mathbf{a}, \mathbf{b}, \mathbf{c}, \mathbf{d})) = \frac{1}{6} \cdot \det(\mathbf{a} - \mathbf{d}, \mathbf{b} - \mathbf{d}, \mathbf{c} - \mathbf{d}).$$

For ACTIVE ANKLE, the simplices

$$\begin{aligned} S_{23} &= \Delta(\mathbf{c}_2, \mathbf{e}_2, \mathbf{c}_3, \mathbf{e}_3) & S_{24} &= \Delta(\mathbf{c}_2, \mathbf{e}_2, \mathbf{c}_4, \mathbf{e}_4) \\ S_{45} &= \Delta(\mathbf{c}_4, \mathbf{e}_4, \mathbf{c}_5, \mathbf{e}_5) & S_{46} &= \Delta(\mathbf{c}_4, \mathbf{e}_4, \mathbf{c}_6, \mathbf{e}_6) \\ S_{61} &= \Delta(\mathbf{c}_6, \mathbf{e}_6, \mathbf{c}_1, \mathbf{e}_1) & S_{62} &= \Delta(\mathbf{c}_6, \mathbf{e}_6, \mathbf{c}_2, \mathbf{e}_2) \end{aligned}$$

are introduced together with the inequality constraints

$$\begin{aligned} \text{svol}(S_{23}) &> 0 & \text{svol}(S_{24}) &> 0 \\ \text{svol}(S_{45}) &> 0 & \text{svol}(S_{46}) &> 0 \\ \text{svol}(S_{61}) &> 0 & \text{svol}(S_{62}) &> 0, \end{aligned} \quad (28)$$

matching the zero posture signs, to exclude those setups that imply a rod interference and a different assembly mode.

Proximity constraint (PC) Similarly, the end effector point \mathbf{e} is kept nearby the origin $\mathbf{0}$ with the constraint

$$\|\mathbf{e} - \mathbf{0}\|^2 \leq d^2, \quad (29)$$

to exclude the potential ‘upside-down’ assembly mode of the ACTIVE ANKLE from the realizable workspace.

Ball-and-socket constraint (BC) Finally, a constraint is introduced to study the effect of the physical limitations of the employed ball-and-socket joints: let the rod vectors \mathbf{r}_i be defined as $\mathbf{r}_i = \mathbf{e}_i - \mathbf{c}_i$, let the base planes \mathcal{B}_i be defined as $\mathcal{B}_1 = \mathcal{B}_2 = (1, 0, 0)^\perp$, $\mathcal{B}_3 = \mathcal{B}_4 = (0, 1, 0)^\perp$, $\mathcal{B}_5 = \mathcal{B}_6 = (0, 0, 1)^\perp$, and let the effector planes \mathcal{E}_i be defined as $\mathcal{E}_1 = \mathcal{E}_2 = (\mathbf{e}_1 - \mathbf{e}_2)^\perp$, $\mathcal{E}_3 = \mathcal{E}_4 = (\mathbf{e}_3 - \mathbf{e}_4)^\perp$, $\mathcal{E}_5 = \mathcal{E}_6 = (\mathbf{e}_5 - \mathbf{e}_6)^\perp$. With these preparations, the constraints of the passive ball-and-socket joints are expressed by

$$|\angle(\mathbf{r}_i, \mathcal{B}_i)| \leq 25^\circ \quad \wedge \quad |\angle(\mathbf{r}_i, \mathcal{E}_i)| \leq 25^\circ, \quad (30)$$

where the absolute angle in degree $|\angle^\circ|$ between a vector \mathbf{a} and a plane \mathcal{H} , that specified by the plane normal vector \mathbf{n} as $\mathcal{H} = \mathcal{H}(\mathbf{n}) = \mathbf{n}^\perp$, is computed as

$$|\angle^\circ(\mathbf{a}, \mathcal{H}(\mathbf{n}))| = \text{asin}\left(\frac{|\mathbf{a} * \mathbf{n}|}{\|\mathbf{a}\| \cdot \|\mathbf{n}\|}\right) \cdot \frac{360^\circ}{2\pi}.$$

By means of (27–30), the realizability of ACTIVE ANKLE’s configurations can be classified: the workspace limits with respect to *interferences* of links of the mechanism (28, 29) and feasible intervals of *passive* ball-and-socket joints (30) are considered, compare [29]. In the following three-dimensional illustrations, four views are provided to motivate a spatial imagination of all three displayed domains: in each case, the image perspectives

from left-to-right are: (i) ‘from top’ ($\hat{\mathbf{k}}$), (ii) ‘from left’ ($\hat{\mathbf{i}}$), (iii) ‘from slanted above’ ($((1, 1, 1))$), and (iv) ‘from right’ ($\hat{\mathbf{j}}$), compare [5]. The color encoding in Figures 12–17 is defined by a bijection in which colors encode joint configurations: the relation can be read off from Figure 12 and 15 in which the color of a point correlates to its position in the depicted configuration space. The vectors $\mathbf{q} = (q_x, q_y, q_z) \in Q^3$ used for in these illustrations are given given by $Q \approx (-89.0^\circ + z \cdot \frac{178^\circ}{49^\circ} : 0 \leq z \leq 49, z \in \mathbb{Z})$ with $|Q| = 50^3 = 125000$.

4.2.1 Configuration Domain

The workspace projection to the domain of the pseudo vectors $\mathbf{q} = (q_x, q_y, q_z)^T$, encoding the ACTIVE ANKLE’s configurations,

$$\{\mathbf{q} \in Q \mid \text{FKP}(\mathbf{q}) = \mathbf{P}_E, \mathbf{P}_E \in SE(3)\}, \quad (31)$$

is first illustrated in a sliced manner in Table 7: from the table, information about the boundaries of the feasible configuration domain of ACTIVE ANKLE are deduced. It is further observed that the feasible set is line symmetric with respect to $(1, 1, 1)$, but *not* point symmetric with respect to the zero configuration $(0, 0, 0) \in Q$. Spatial images of the configuration domain are provided in Figure 12 and Figure 15. The angles q_x , q_y , and q_z in Figure 15 lay in the range $[23.61^\circ, 23.61^\circ]$, instead of $[45.41^\circ, 41.78^\circ]$ in Figure 12 (Table 8), due to the ball-and-socket constraint (30) $(-45.41^\circ, -23.61^\circ, 23.61^\circ, 41.78^\circ \in Q)$.

4.2.2 Translative Domain

The workspace of the ACTIVE ANKLE in the translative domain

$$\{\mathbf{p} \in \mathbb{R}^3 \mid \text{FKP}(\mathbf{q}) = \mathbf{P}_E, \mathbf{P}_E = \begin{pmatrix} \mathbf{R} & \mathbf{p} \\ \mathbf{0} & 1 \end{pmatrix} \in SE(3)\} \quad (32)$$

is depicted in Figure 13 and Figure 16. Together with the numerical data in Table 7, the images indicate that the end effector shift takes place within the positive octant of the global coordinate system O (see Figure 5). Using the ball-and-socket joints with a cone angle of $\pm 25^\circ$ (30), the end-effector shift is restricted by the (loose) upper bound of $\sqrt{3} \cdot 2.53\text{mm} \approx 4.38\text{mm}$.

4.2.3 Rotative Domain

For depicting the workspace within the rotative domain, the angle–axis representation is employed:

$$\begin{aligned} \{\phi \cdot \hat{\mathbf{u}} \in \mathbb{R}^3 \mid \exp(\phi \cdot \hat{\mathbf{u}}^\circ) = \mathbf{R}, \phi \in [0, \pi], \\ \text{FKP}(\mathbf{q}) = \mathbf{P}_E, \mathbf{P}_E = \begin{pmatrix} \mathbf{R} & \mathbf{p} \\ \mathbf{0} & 1 \end{pmatrix} \in SE(3)\} \end{aligned} \quad (33)$$

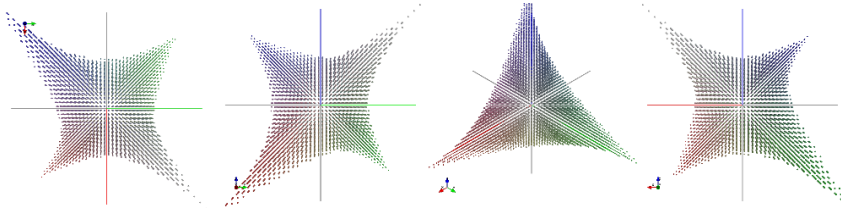


Fig. 12: Visualization of the feasible workspace in joint configuration domain. The set of feasible joint angles $\{ \mathbf{q} \}$ has a ‘simplex-like’ shape with ‘curved’ facets in the joint configuration space \mathcal{Q} (compare to Table 7).

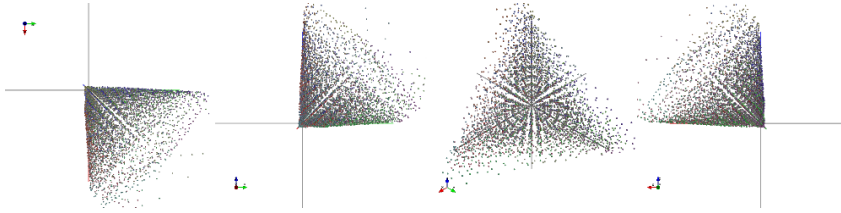


Fig. 13: Visualization of the feasible workspace in translative domain. The set of feasible positions $\{ \mathbf{e} \}$ has a ‘cone-like’ shape and is contained in the positive octant of the coordinate system.

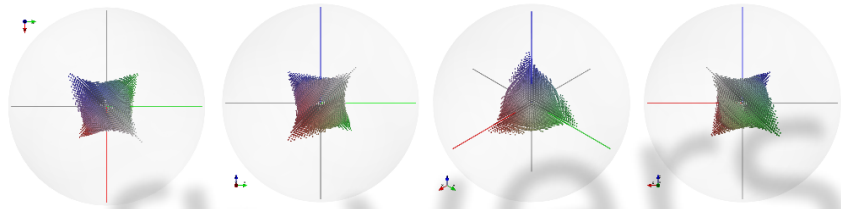


Fig. 14: Visualization of the feasible workspace in rotative domain. The set of feasible orientations $\{ \phi \cdot \hat{\mathbf{u}} \}$, expressed in angle-axis representation, has line-symmetric shape with respect to the axis $(1, 1, 1)^T$.

In the rotative domain, the $(1, 1, 1)$ -symmetric set in Figure 14 has a simplex-like shape that intersects the joint axes at -45.88° and 42.12° (Table 8). The reduced set, cut by the ball-and-socket constraints (30), depicted in Figure 17, has a cube-like shape with side lengths of about $2 \cdot 23.61^\circ$ (Table 8).

Numerical data. An overview of the numerical data of Figures 12–17 is provided in Table 8. Due to the 3-symmetric design of the ACTIVE ANKLE, the numerical values are identical for all three axes in all three domains.

5 ROM Analysis and Control of Active Ankle

ACTIVE ANKLE is used as a 3 DOF active spherical module at hip and ankle joints in the RECUPERA full body exoskeleton, as shown in Figure 18. This section presents the range of motion (ROM) analysis of the ACTIVE ANKLE and the experimental results of its kinematic control based on the Rotative Inverse Kinematic Model (RIKM) from Section 3.3. For sake of brevity, the results are only reported for its application as an ankle joint.

Table 8: Overview of numerical values of the two datasets: Dataset \mathcal{A} is constrained by (27–29) and contains 9843 samples, dataset \mathcal{B} is constrained by (27–30) and contains 2478 samples. The terms l_p and u_p indicate the plot ranges, l_c and u_c represent maximal coordinates of the point clouds, and l_a and u_a indicate intersections of clouds’ surfaces with coordinate axes.

Domain	Configuration	Translative	Rotative
$[l_p, u_p]$	$[-90^\circ, 90^\circ]$	$[-3.5 \text{ mm}, 3.5 \text{ mm}]$	$[-180^\circ, 180^\circ]$
Dataset \mathcal{A}			
	Figure 12	Figure 13	Figure 14
$[l_c, u_c]$	$[-78.10^\circ, 78.10^\circ]$	$[0 \text{ mm}, 4.87 \text{ mm}]$	$[-65.27^\circ, 62.92^\circ]$
$[l_a, u_a]$	$[-45.41^\circ, 41.78^\circ]$	$[0 \text{ mm}, 1.37 \text{ mm}]$	$[-45.88^\circ, 42.12^\circ]$
Dataset \mathcal{B}			
	Figure 15	Figure 16	Figure 17
$[l_c, u_c]$	$[-23.61^\circ, 23.61^\circ]$	$[0 \text{ mm}, 2.53 \text{ mm}]$	$[-31.25^\circ, 31.95^\circ]$
$[l_a, u_a]$	$[-23.61^\circ, 23.61^\circ]$	$[0 \text{ mm}, 1.03 \text{ mm}]$	$[-23.61^\circ, 23.61^\circ]$

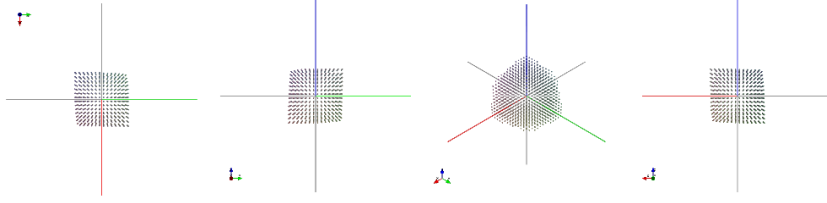


Fig. 15: Visualization of the feasible workspace in joint configuration domain restricted by the ball-and-socket constraint (30). The set of feasible joint angles $\{\mathbf{q}\}$ has a ‘cube-like’ shape in the joint configuration space \mathcal{Q} (compare to Figure 12).

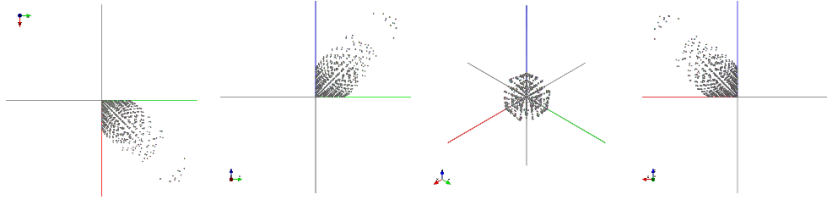


Fig. 16: Visualization of the feasible workspace in translative domain restricted by the ball-and-socket constraint (30). The set of feasible positions $\{\mathbf{e}\}$ has a ‘pen-like’ shape contained in the positive octant of the coordinate system (compare to Figure 13).

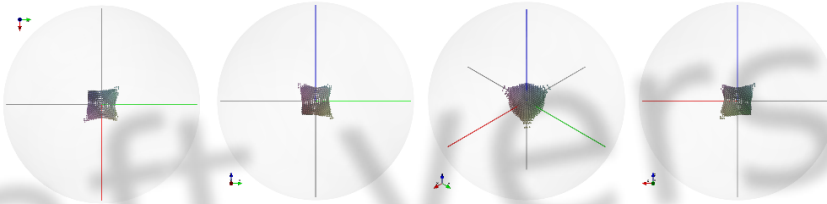


Fig. 17: Visualization of the feasible workspace in rotative domain, restricted by the ball-and-socket constraint (30). The set of feasible orientations $\{\phi \cdot \hat{\mathbf{u}}\}$ has the shape of a deformed cube (compare to Figure 14).

5.1 Range of motion analysis

The three primary motions available at the human ankle (dorsiflexion–plantarflexion ϕ_α , eversion–inversion ϕ_β , and adduction–abduction ϕ_γ) are shown in Figure 20. Their overall ranges of motion are shown in Table 9. During most activities of daily living, only a partial ROM is required: walking on an even surface ($10^\circ - 15^\circ$ plantar flexion and 10° dorsiflexion), walking upstairs (37° total ROM), walking downstairs (56° total ROM) [36].

To demonstrate the suitability of ACTIVE ANKLE mechanism for human ankle related applications (see Figure 19), these movements have been performed on this mechanism using RIKM and its ROM has been evaluated. The ROM offered by the ACTIVE ANKLE is subjected to the physical motion limits of the ball and socket joints. For the presented prototype in Figure 1, the ball and socket joints used have a motion range of $\pm 25^\circ$. Thus, the maximum possible motion range for the three rotative joints ($J_{01,12}$, $J_{01,32}$, and $J_{01,52}$) lays

between -25° and $+25^\circ$. The three task space trajectories in angle-axis representation, where ω represent the angular speed and t is the time, are selected.

$$\begin{aligned} \mathbf{u}_\alpha &= (+1, -1, -1)^T, & \phi_\alpha &= 28.65^\circ \cdot \sin(\omega \cdot t) + 8.65^\circ \\ \mathbf{u}_\beta &= (+1, +1, -1)^T, & \phi_\beta &= 25.00^\circ \cdot \sin(\omega \cdot t) + 10.0^\circ \\ \mathbf{u}_\gamma &= (+1, +1, +1)^T, & \phi_\gamma &= 33.59^\circ \cdot \sin(\omega \cdot t) + 3.44^\circ \end{aligned}$$

Table 9: Comparison of primary motion ranges, dorsiflexion – plantarflexion (DF–PF), eversion–inversion (EV–IV), and adduction–abduction (AD–AB), at human and ACTIVE ANKLE.

Motion type	Human Ankle			ACTIVE ANKLE		
	min.	max.	abs.	min.	max.	abs.
DF – PF	-20°	50°	70°	-19.83°	37.23°	57.06°
EV – IV	-15°	35°	50°	-15.00°	35.00°	50.00°
AD – AB	-30°	45°	75°	-29.20°	36.96°	66.16°

The input joint angles needed to perform these motions are plotted against the task space angles (ϕ_α , ϕ_β , ϕ_γ) in Figures 21–23. The end effector shift encountered while performing these motions have been shown in Figures 24–26. In all cases, it can be observed that the shifts are less than 1 mm in magnitude and hence practically insignificant. The available ROM constrained by the physical limits of the ball and socket joints are shown against the human ankle ROM in Table 9. It is evident that the presented design can fulfill the range of motion required for most day to day activities. These results show the suitability of ACTIVE ANKLE in full body exoskeletons, ankle rehabilitation devices, and humanoid robots.

5.2 Kinematic Control Experiments

The Rotative Inverse Kinematic Model (RIKM) has been implemented within the real time *Robot Construction Kit* (RoCK) [18] to achieve a kinematic control of the ACTIVE ANKLE. For a tolerance of $\epsilon = 1.e^{-06}$ mm, the algorithm converges in four to six iterations, can be implemented with a control loop frequency of 1 kHz, and is thus suitable for most applications from a control perspective. The kinematic control of ACTIVE ANKLE is implemented on a mid-level control PC communicating with the FPGA electronics of the actuators which implement low level cascaded position, velocity, and torque controllers. These low level controllers ensure safety limits at position, velocity and current levels in any selected control mode [2].

To demonstrate the performance of the kinematic control, the following three task space trajectories corresponding to dorsiflexion–plantarflexion ϕ_α , eversion–inversion ϕ_β , and adduction–abduction ϕ_γ movements are selected:

$$\begin{aligned} \mathbf{u}_\alpha &= (+1, -1, -1)^T, & \phi_\alpha &= 17.19^\circ \cdot \sin(\omega \cdot t) + 5.19^\circ \\ \mathbf{u}_\beta &= (+1, +1, -1)^T, & \phi_\beta &= 18.69^\circ \cdot \sin(\omega \cdot t) + 7.44^\circ \\ \mathbf{u}_\gamma &= (+1, +1, +1)^T, & \phi_\gamma &= 25.19^\circ \cdot \sin(\omega \cdot t) + 2.58^\circ \end{aligned}$$

The tracking during the three aforementioned trajectories is shown in Figures 27–29 where $(\tilde{q}_x, \tilde{q}_y, \tilde{q}_z)$ are the desired input trajectories to the joints and (q_x, q_y, q_z) demonstrate the real joint states. The maximum absolute errors between desired and real joint trajectories of the three actuators, calculated as $q_e = \max(|\tilde{q}_x - q_x|, |\tilde{q}_y - q_y|, |\tilde{q}_z - q_z|)$, during the dorsiflexion–plantarflexion, eversion–inversion and adduction–abduction movements are 0.61° , 0.79° , and 0.23° , respectively. The maximum of the mean absolute errors of the three actuators during the three movements are 0.37° , 0.47° , and 0.09° , respectively. These figures demonstrates the robustness of the low level controller.

6 Conclusion and Outlook

This article presents crucial aspects of the ACTIVE ANKLE, a novel parallel manipulator with mobility three that moves in an almost spherical manner. The design considerations, specifications, and the inverse and forward kinematic models are presented, unveiling its distinctive features and its suitability as a spherical joint module in an exoskeleton. For each of the kinematic problems, a detailed algorithmic treatment is provided. The kinematic control of ACTIVE ANKLE is presented with a comparison of its motion range to that of a human ankle joint. The primary application of this almost-spherical parallel mechanism is an active spherical joint module where small translations of the endeffector can be tolerated. Alternately, it may also be integrated as a submechanism together with a regional manipulator for obtaining precise six DOF motions. Here, its translations need to be compensated by the other joints of the overall device. In the future, the modeling of the mechanism can be extended to include its instantaneous kinematics and dynamics due to a computationally efficient rotative inverse kinematic model. A cascaded position, velocity, and torque controller in the $SO(3)$ task-space will enable an ideal almost-spherical mechanism for diverse applications. Equipped with a modular controller implemented on an embedded processor, the ACTIVE ANKLE will serve as a versatile, active 3-DOF spherical joint within a full-body hybrid serial-parallel exoskeleton.

A Reference Configurations

A set of reference configurations of the mechanism ACTIVE ANKLE is displayed in Table 10.

B Sphere Intersection Problem

The method SPHINT in Alg. 9, called from Alg. 5, computes the intersection of three spheres using distance geometry. It is based on the *quadrance* [42] between two vectors \mathbf{a} and \mathbf{b} ,

$$Q(\mathbf{a}, \mathbf{b}) = (\mathbf{b} - \mathbf{a}) * (\mathbf{b} - \mathbf{a}),$$

the squared distance between \mathbf{a} and \mathbf{b} , and its generalization to vector sets, the Cayley–Menger bideterminants [38].

C Representation Conversion Methods

The conversion methods MAT2VEC and VEC2MAT, called from Alg. 7 and Alg. 8, are stated in Alg. 12 and Alg. 13.



Fig. 18: ACTIVE ANKLE applied as 3-DOF hip and ankle joints in the RECUPERA full body exoskeleton.

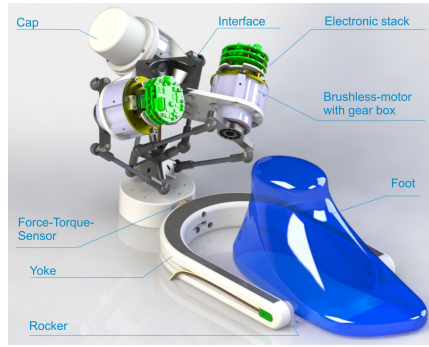


Fig. 19: Integration of ACTIVE ANKLE as a foot unit of an exoskeleton, with motors, sensors, and electronics.

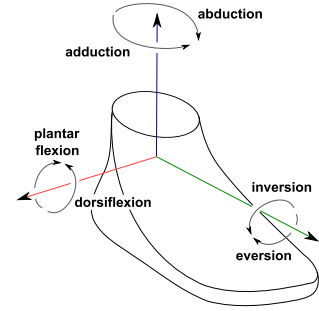


Fig. 20: Illustration of the three primary rotations of the human ankle joint.

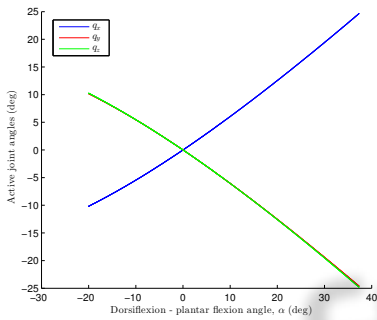


Fig. 21: Active Joint angles during dorsiflexion – plantarflexion motion.

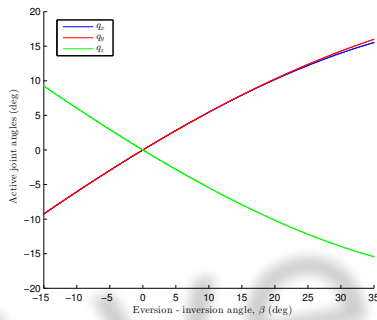


Fig. 22: Active joint angles during the eversion – inversion motion.

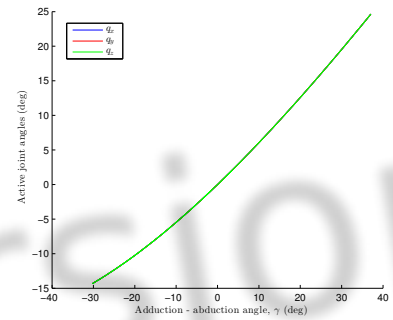


Fig. 23: Active joint angles during the adduction – abduction motion.

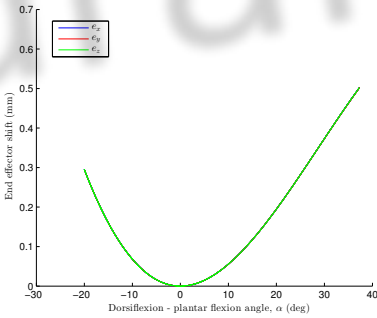


Fig. 24: End effector shift during the dorsiflexion – plantarflexion motion.

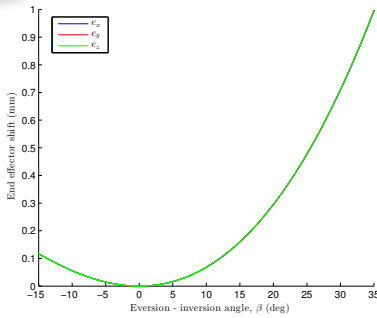


Fig. 25: End effector shift during the eversion – inversion motion.

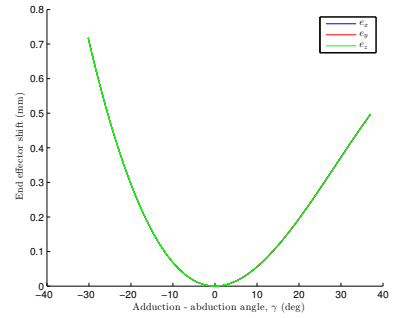


Fig. 26: End effector shift during the adduction – abduction motion.

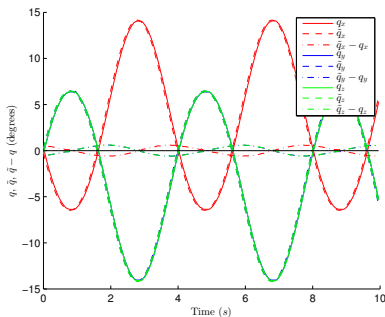


Fig. 27: Trajectory tracking during dorsiflexion – plantarflexion motion.

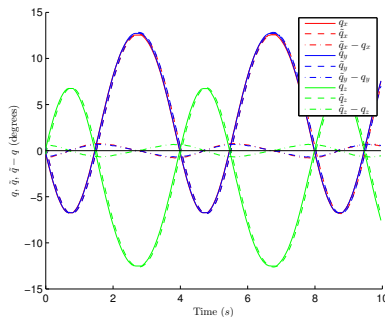


Fig. 28: Trajectory tracking during the eversion – inversion motion.

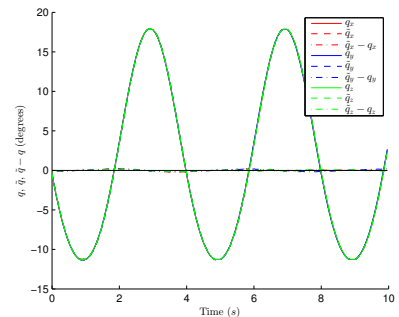


Fig. 29: Trajectory tracking during the adduction – abduction motion.

Table 10: Reference configurations with joint angles, end-effector poses, and point coordinates

Ind.	Joint angles $\mathbf{q} = (q_x, q_y, q_z)$	Position \mathbf{e}	Orientation		Effector points			Crank points		
			ϕ	$\hat{\mathbf{u}}$	$\mathbf{e}_1^T, \mathbf{e}_3^T, \mathbf{e}_5^T$	$\mathbf{e}_2^T, \mathbf{e}_4^T, \mathbf{e}_6^T$	$\mathbf{c}_1^T, \mathbf{c}_3^T, \mathbf{c}_5^T$	$\mathbf{c}_2^T, \mathbf{c}_4^T, \mathbf{c}_6^T$		
1	$(0^\circ, 0^\circ, 0^\circ)$	$\begin{pmatrix} 0 \\ 0 \\ 0 \end{pmatrix}$	0°	$\begin{pmatrix} 0 \\ 1 \\ 0 \end{pmatrix}$	$(0, 35, 0)$ $(0, 0, 35)$ $(35, 0, 0)$	$(0, -35, 0)$ $(0, 0, -35)$ $(-35, 0, 0)$	$(0, 35, 100)$ $(100, 0, 35)$ $(35, 100, 0)$	$(0, -35, 100)$ $(100, 0, -35)$ $(-35, 100, 0)$		
2	$(-5^\circ, 0^\circ, 0^\circ)$	$\begin{pmatrix} 0.047 \\ 0 \\ 0 \end{pmatrix}$	-5°	$\begin{pmatrix} 1 \\ 0 \\ 0 \end{pmatrix}$	$(0.047, 34.867, -3.05)$ $(0.047, 3.05, 34.867)$ $(35.047, 0, 0)$	$(0.047, -34.867, 3.05)$ $(0.047, -3.05, -34.867)$ $(-34.953, 0, 0)$	$(0, 34.867, 96.95)$ $(100, 0, 35)$ $(35, 100, 0)$	$(0, -34.867, 103.05)$ $(100, 0, -35)$ $(-35, 100, 0)$		
3	$(0^\circ, 10^\circ, 0^\circ)$	$\begin{pmatrix} 0 \\ 0.186 \\ 0 \end{pmatrix}$	10°	$\begin{pmatrix} 0 \\ 1 \\ 0 \end{pmatrix}$	$(0, 35.186, 0)$ $(6.078, 0.186, 34.468)$ $(34.468, 0.186, -6.078)$	$(0, -34.814, 0)$ $(-6.078, 0.186, -34.468)$ $(-34.468, 0.186, 6.078)$	$(0, 35, 100)$ $(106.078, 0, 34.468)$ $(35, 100, 0)$	$(0, -35, 100)$ $(93.922, 0, -34.468)$ $(-35, 100, 0)$		
4	$(0^\circ, 0^\circ, 15^\circ)$	$\begin{pmatrix} 0.001 \\ 0.001 \\ 0.418 \end{pmatrix}$	15°	$\begin{pmatrix} 0 \\ 0 \\ 1 \end{pmatrix}$	$(-9.058, 33.808, 0.418)$ $(0.001, 0.001, 35.418)$ $(33.808, 9.06, 0.418)$	$(9.06, -33.807, 0.418)$ $(0.001, 0.001, -34.582)$ $(-33.807, -9.058, 0.418)$	$(0, 35, 100)$ $(100, 0, 35)$ $(33.807, 109.059, 0)$	$(0, -35, 100)$ $(100, 0, -35)$ $(-33.807, 90.941, 0)$		
5	$(5^\circ, 10^\circ, 15^\circ)$	$\begin{pmatrix} 0.013 \\ 0.152 \\ 0.381 \end{pmatrix}$	17.991°	$\begin{pmatrix} 0.213 \\ 0.534 \\ 0.818 \end{pmatrix}$	$(-8.636, 33.929, 3.428)$ $(6.088, -1.399, 34.815)$ $(33.379, 9.19, -5.099)$	$(8.662, -33.625, -2.667)$ $(-6.062, 1.703, -34.053)$ $(-33.353, -8.886, 5.86)$	$(0, 34.867, 103.05)$ $(106.078, 0, 34.468)$ $(33.807, 109.059, 0)$	$(0, -34.867, 96.95)$ $(93.922, 0, -34.468)$ $(-33.807, 90.941, 0)$		
6	$(-5^\circ, -3^\circ, -1^\circ)$	$\begin{pmatrix} 0.048 \\ 0.018 \\ 0.003 \end{pmatrix}$	-5.995°	$\begin{pmatrix} 0.839 \\ 0.509 \\ 0.189 \end{pmatrix}$	$(0.822, 34.876, -3.047)$ $(-1.783, 3.105, 34.818)$ $(34.991, -0.593, 1.895)$	$(-0.727, -34.84, 3.053)$ $(1.879, -3.069, -34.812)$ $(-34.896, 0.629, -1.889)$	$(0, 34.867, 96.95)$ $(98.168, 0, 34.952)$ $(34.995, 99.389, 0)$	$(0, -34.867, 103.05)$ $(101.832, 0, -34.952)$ $(-34.995, 100.611, 0)$		

Algorithm 9 Intersection of three spheres (SPHINT)**Require:** Spheres; midpoints $\mathbf{m}_1, \mathbf{m}_2, \mathbf{m}_3$ and radii r_1, r_2, r_3 **Ensure:** Intersection; points \mathbf{p}_+ and \mathbf{p}_- , with $\|\mathbf{p}_+ - \mathbf{s}_i\| = r_i$ and $\|\mathbf{p}_- - \mathbf{s}_i\| = r_i$ for $i \in \{1, 2, 3\}$, or empty set

```

1: function SPHINT( $\mathbf{m}_1, \mathbf{m}_2, \mathbf{m}_3, r_1, r_2, r_3$ )
2:    $R_1 \leftarrow r_1^2, R_2 \leftarrow r_2^2, R_3 \leftarrow r_3^2$ 
3:    $\mathbf{Q} \leftarrow \begin{pmatrix} 0 & 1 & 1 & 1 & 1 \\ 1 & 0 & Q(\mathbf{m}_1, \mathbf{m}_2) & Q(\mathbf{m}_1, \mathbf{m}_3) & R_1 \\ 1 & Q(\mathbf{m}_2, \mathbf{m}_1) & 0 & Q(\mathbf{m}_2, \mathbf{m}_3) & R_2 \\ 1 & Q(\mathbf{m}_3, \mathbf{m}_1) & Q(\mathbf{m}_3, \mathbf{m}_2) & 0 & R_3 \\ 1 & R_1 & R_2 & R_3 & 0 \end{pmatrix}$ 
4:    $D_{(1234)} \leftarrow \frac{1}{8} \cdot \det(\mathbf{Q})$   $\triangleright$  CM determinant
5:   if  $D_{(1234)} < 0$  then  $\triangleright$  Empty intersection
6:     return  $\emptyset$ 
7:    $D_{(123)} \leftarrow -\frac{1}{4} \cdot \text{MINOR}(\mathbf{Q}, (0, 1, 2, 3), (0, 1, 2, 3), 0)$ 
8:    $D_{(123;124)} \leftarrow -\frac{1}{4} \cdot \text{MINOR}(\mathbf{Q}, (0, 1, 2, 3), (0, 1, 2, 4), 0)$ 
9:    $D_{(123;134)} \leftarrow -\frac{1}{4} \cdot \text{MINOR}(\mathbf{Q}, (0, 1, 2, 3), (0, 1, 3, 4), 0)$ 
10:   $\mathbf{v}_1 \leftarrow \mathbf{m}_2 - \mathbf{m}_1$ 
11:   $\mathbf{v}_2 \leftarrow \mathbf{m}_3 - \mathbf{m}_1$ 
12:   $\mathbf{v}_0 \leftarrow -D_{(123;134)} \cdot \mathbf{v}_1 + D_{(123;124)} \cdot \mathbf{v}_2$ 
13:   $\mathbf{v}_\Delta \leftarrow \sqrt{D_{(1234)}} \cdot (\mathbf{v}_1 \times \mathbf{v}_2)$ 
14:   $\mathbf{p}_+ \leftarrow \mathbf{m}_1 + \frac{1}{D_{(123)}} \cdot (\mathbf{v}_0 + \mathbf{v}_\Delta)$ 
15:   $\mathbf{p}_- \leftarrow \mathbf{m}_1 + \frac{1}{D_{(123)}} \cdot (\mathbf{v}_0 - \mathbf{v}_\Delta)$ 
16:  return  $\mathbf{p}_+, \mathbf{p}_-$ 

```

Algorithm 12 Conv. from pose matrix to pose vector**Require:** Pose matrix $\mathbf{P} \in SE(3)$ **Ensure:** Pose vector $\mathbf{x} = (\phi, u_x, u_y, u_z, p_x, p_y, p_z)^T$

```

1: function MAT2VEC( $\mathbf{P}$ )
2:    $\begin{pmatrix} \mathbf{R} & \mathbf{p} \\ \mathbf{0} & 1 \end{pmatrix} \leftarrow \mathbf{P}$ 
3:    $\phi \leftarrow \arccos\left(\frac{\text{tr}(\mathbf{R})-1}{2}\right) \in [0, \pi]$ 
4:    $\hat{\mathbf{u}} \leftarrow \begin{cases} ((\mathbf{R} - \mathbf{R}^T)^\oplus)^\circ & \phi \neq \pi \\ \text{diag}(\frac{1}{2} \cdot (\mathbf{R} + \mathbf{I}))^\circ \frac{1}{2} & \phi = \pi \end{cases}$ 
5:    $(u_x, u_y, u_z) \leftarrow \hat{\mathbf{u}}$ 
6:    $(p_x, p_y, p_z) \leftarrow \mathbf{p}$ 
7:    $\mathbf{x} \leftarrow (\phi, u_x, u_y, u_z, p_x, p_y, p_z)^T$ 
8:   return  $\mathbf{x}$ 

```

Algorithm 10 Matrix minor (MINOR)**Require:** Matrix $\mathbf{A} \in \mathbb{R}^{m \times n}$, row indices $R = (r_1, r_2, \dots, r_p)$, column indices $C = (c_1, c_2, \dots, c_q)$, $x \in \{0, 1\}$ **Ensure:** Determinant of the submatrix $\mathbf{A}_{[R][C]} \in \mathbb{R}^{p \times q}$

```

1: function MINOR( $\mathbf{A}, R, C, x$ )
2:   if  $x = 0$  then  $\triangleright$  Index handling
3:     do  $r_i \leftarrow r_i + 1$  for  $r_i \in R$ 
4:     do  $c_j \leftarrow c_j + 1$  for  $c_j \in C$ 
5:    $\mathbf{A}_{[R][C]} \leftarrow \text{EXTRACT}(\mathbf{A}, R, C)$   $\triangleright$  Submatrix
6:    $m \leftarrow \det(\mathbf{A}_{[R][C]})$   $\triangleright$  Minor
7:   return  $m$ 

```

Algorithm 11 Submatrix extraction (EXTRACT)**Require:** Matrix $\mathbf{A} \in \mathbb{R}^{m \times n}$, row indices $R = (r_1, r_2, \dots, r_p)$ with $1 \leq r_i \leq m$ for $1 \leq i \leq p$, and column indices $C = (c_1, c_2, \dots, c_q)$ with $1 \leq r_j \leq n$ for $1 \leq j \leq q$ **Ensure:** Submatrix $\mathbf{A}_{[R][C]} \in \mathbb{R}^{p \times q}$ extracted by R and C

```

1: function EXTRACT( $\mathbf{A}, R, C$ )
2:    $\mathbf{R} \leftarrow ({}^m \hat{\mathbf{e}}_{r_1} \quad {}^m \hat{\mathbf{e}}_{r_2} \quad \dots \quad {}^m \hat{\mathbf{e}}_{r_p})^T$   $\triangleright \mathbf{R} \in \mathbb{R}^{p \times m}$ 
3:    $\mathbf{C} \leftarrow ({}^n \hat{\mathbf{e}}_{c_1} \quad {}^n \hat{\mathbf{e}}_{c_2} \quad \dots \quad {}^n \hat{\mathbf{e}}_{c_q})$   $\triangleright \mathbf{C} \in \mathbb{R}^{n \times q}$ 
4:    $\mathbf{A}_{[R][C]} \leftarrow \mathbf{R} \cdot \mathbf{A} \cdot \mathbf{C}$ 
5:   return  $\mathbf{A}_{[R][C]}$ 

```

Algorithm 13 Conv. from pose vector to pose matrix**Require:** Pose vector $\mathbf{x} = (\phi, u_x, u_y, u_z, p_x, p_y, p_z)$ **Ensure:** Pose matrix $\mathbf{P} \in SE(3)$

```

1: function VEC2MAT( $\phi, u_x, u_y, u_z, p_x, p_y, p_z$ )
2:    $\hat{\mathbf{u}} \leftarrow (u_x, u_y, u_z)^T$ 
3:    $\mathbf{p} \leftarrow (p_x, p_y, p_z)^T$ 
4:    $\mathbf{R} \leftarrow \exp(\phi \cdot \hat{\mathbf{u}}^\otimes)$ 
5:    $\mathbf{P} \leftarrow \begin{pmatrix} \mathbf{R} & \mathbf{p} \\ \mathbf{0} & 1 \end{pmatrix}$ 
6:   return  $\mathbf{P}$ 

```

References

1. K. Al-Widyan, X. Q. Ma, and J. Angeles. The robust design of parallel spherical robots. *Mechanism and Machine Theory*, 46(3):335–343, 2011.
2. Vinzenz Bargsten and Jose de Gea Fernandez. Compi: Development of a 6-dof compliant robot arm for human-robot cooperation. In *Proceedings of the 8th International Workshop on Human-Friendly Robotics*. TU München, 2015.
3. Luc Baron. A joint-limits avoidance strategy for arc-welding robots. In *Integrated Design and Manufacturing in Mechanical Engineering*, 2000.
4. Oriol Bohigas, Montserrat Manubens, and Llus Ros. Singularities of non-redundant manipulators: A short account and a method for their computation in the planar case. *Mechanism and Machine Theory*, 68(0):1–17, 2013.
5. Bertold Bongardt. Geometric characterization of the workspace of non-orthogonal rotation axes. *J. of Geometric Mechanics*, 6(2):141–166, 2014.
6. Bertold Bongardt. Inverse kinematics of anthropomorphic arms yielding eight coinciding circles. In *International Workshop on Computational Kinematics*, 2017.
7. J. Brinker and B. Corves. A survey on parallel robots with delta-like architecture. In *IFTToMM World Congress*, 2015.
8. Sébastien Briot, Anatoly Pashkevich, and Damien Chablat. On the optimal design of parallel robots taking into account their deformations and natural frequencies. *CoRR*, 2009.
9. R. Clavel. *Conception d'un robot parallèle rapide à 4 degrés de liberté*. PhD thesis, EPFL Lausanne, 1991.
10. J. K. Davidson, K. H. Hunt, and G. R. Pennock. *Robots and Screw Theory: Applications of Kinematics and Statics to Robotics*. 2004.
11. Roy Featherstone. *Rigid Body Dynamics Algorithms*. Springer, 2008.
12. M. Frindt. *Modulbasierte Synthese von Parallelstrukturen für Maschinen in der Produktionstechnik*. PhD thesis, Technical University of Braunschweig, 2001.
13. Jaime Gallardo-Alvarado. *Kinematic Analysis of Parallel Manipulators by Algebraic Screw Theory*. 1 edition, 2016.
14. R. A. R. C. Gopura, K. Kiguchi, and D. S. V. Bandara. A brief review on upper extremity robotic exoskeleton systems. In *2011 6th International Conference on Industrial and Information Systems*, pages 346–351, Aug 2011.
15. C. Gosselin, E. St-Pierre, and M. Gagne. On the development of the agile eye: mechanical design, control issues and experimentation. *IEEE Robotics and Automation Society Magazine*, 3(4), 1996.
16. Hugh Herr. Exoskeletons and orthoses: classification, design challenges and future directions. *J. of NeuroEngineering and Rehabilitation*, 6(1):21, 2009.
17. J. Huang, X. Tu, and J. He. Design and evaluation of the rupert wearable upper extremity exoskeleton robot for clinical and in-home therapies. *IEEE Transactions on Systems, Man, and Cybernetics: Systems*, 46(7):926–935, July 2016.
18. Sylvain Joyeux and Jan Albiez. Robot development: from components to systems. In *6th National Conference on Control Architectures of Robots, Grenoble, France*, 2011.
19. Alfred B. Kempe. *How to Draw a Straight Line*. 1877.
20. Wisama Khalil and Etienne Dombre. *Modeling, Identification and Control of Robots*. Taylor and Francis, 2002.
21. Wisama Khalil and Etienne Dombre. *Modeling, Identification and Control of Robots*. Taylor & Francis, Inc., Bristol, PA, USA, 3rd edition, 2002.
22. E. A. Kirchner, N. Will, M. Simnofske, L. M. Vaca Benitez, B. Bongardt, M. M. Krell, S. Kumar, M. Mallwitz, A. Seeland, M. Tabie, H. Woehrl, M. Yueksel, A. Hess, R. Buschfort, and F. Kirchner. Recupera-reha: Exoskeleton technology with integrated biosignal analysis for sensorimotor rehabilitation. In *Transdisziplinäre Konferenz SmartASSIST*, pages 504–517, 2016.
23. Xianwen Kong and Clément M. Gosselin. *Type Synthesis of Parallel Mechanisms*. 2007.
24. S. Kumar, A. Nayak, B. Bongardt, A. Mueller, and F. Kirchner. *Kinematic Analysis of Active Ankle Using Computational Algebraic Geometry*, pages 117–125. Cham, 2018.
25. Shivesh Kumar, Marc Simnofske, Bertold Bongardt, Andreas Müller, and Frank Kirchner. Integrating mimic joints into dynamics algorithms: Exemplified by the hybrid recupera exoskeleton. In *Proceedings of the Advances in Robotics, AIR '17*, pages 27:1–27:6, New York, NY, USA, 2017. ACM.
26. Weimin Li, Feng Gao, and Jianjun Zhang. A three-dof translational manipulator with decoupled geometry. 23:805–808, 2005.
27. L. Luzi, N. Sancisi, and V. Parenti Castelli. A new direct position analysis solution for an over-constrained gough-stewart platform. In *Computational Kinematics*, 2017.

28. J. P. Merlet. Parallel manipulators: state of the art and perspectives. *Advanced Robotics*, 1993.
 29. J.-P. Merlet. Determination of the orientation workspace of parallel manipulators. *J. of intelligent and robotic systems*, 13(2):143–160, 1995.
 30. Tobias Nef, Marco Guidali, Verena Klamroth-Marganska, and Robert Riener. *ARMin - Exoskeleton Robot for Stroke Rehabilitation*, pages 127–130. 2009.
 31. A. Niyetkaliyev and A. Shintemirov. An approach for obtaining unique kinematic solutions of a spherical parallel manipulator. In *IEEE/ASME International Conference on Advanced Intelligent Mechatronics (AIM)*, pages 1355–1360, 7 2014.
 32. Gregory S. Sawicki and Daniel P. Ferris. A pneumatically powered knee-ankle-foot orthosis (kafo) with myoelectric activation and inhibition. *J. of NeuroEngineering and Rehabilitation*, 6(1):23, 2009.
 33. J.M. Selig and Hui Li. A geometric newton-raphson method for gough-stewart platforms. In *Computational Kinematics*, pages 183–190. 2009.
 34. M. Simnofske. Ausrichtungsvorrichtung zum Ausrichten einer Plattform in drei rotatorischen Freiheiten. Patent appl. DE102013018034A1, 2015.
 35. M. Simnofske, S. Kumar, B. Bongardt, and F. Kirchner. Active ankle - an almost-spherical parallel mechanism. In *47th International Symposium on Robotics (ISR)*, June 2016.
 36. R. N. Stauffer, E. Y. S. Chao, and R. C. Brewster. Force and motion analysis of the normal, diseased, and prosthetic ankle joint. *Clinical Orthopaedics and Related Research*, 127(127):189–96, 1977.
 37. R. K. G. Temple. The cardan suspension. *The UNESCO Courier*, 1988.
 38. Federico Thomas and Llus Ros. Revisiting trilateration for robot localization. *IEEE Transactions on Robotics*, 21(1):93–101, 2005.
 39. M. Valasek, J. Zicha, M. Karasek, and R. Hudec. Hexasphere – redundantly actuated parallel spherical mechanism as a new concept of agile telescope. *Advances in Astronomy*, 2010.
 40. T. Villgrattner, E. Schneider, P. Andersch, and H. Ulbrich. Compact high dynamic 3 dof camera orientation system: Development and control. *J. of System Design and Dynamics*, 5(5):819–828, 2011.
 41. P. Vischer and R. Clavel. Argos: A novel 3-dof parallel wrist mechanism. *The International Journal of Robotics Research*, 19(1):5–11, 2000.
 42. Norman J. Wildberger. A Rational Approach to Trigonometry. *Math Horizons*, 2007.
 43. G. Wu. Kinematic analysis and optimal design of a wall-mounted four-limb parallel schoenflies-motion robot for pick-and-place operations. *Journal of Intelligent and Robotic Systems*, pages 1–15, 2016.
 44. G. Wu, S. Caro, and J. Wang. Design and transmission analysis of an asymmetrical spherical parallel manipulator. *Mechanism and Machine Theory*, 94:119 – 131, 2015.
 45. S. Yamamoto, A. Hagiwara, T. Mizobe, O. Yokoyama, and T. Yasui. Development of an ankle-foot orthosis with an oil damper. *Prosthetics and Orthotics Int.*, 29(3), 2005.
 46. A. B. Zoss, H. Kazerooni, and A. Chu. Biomechanical design of the berkeley lower extremity exoskeleton (bleex). *IEEE/ASME Transactions on Mechatronics*, 11(2):128–138, April 2006.
- Shivesh Kumar is a researcher at the DFKI Robotics Innovation Center, Bremen. He obtained his Masters degree in Control Engineering, Robotics, and Applied Informatics with specialization in Advanced Robotics from Ecole Centrale de Nantes, France in 2015 and Bachelors degree in Mechanical Engineering from National Institute of Technology Karnataka, India in 2013. His research interests include kinematics, dynamics and control of robots with applications in the fields of exoskeletons, humanoids, rehabilitation and industrial automation.
- Bertold Bongardt studied technical mathematics at the Technical University of Berlin. Since 2008, he has been a researcher at DFKI Robotics Innovation Center, Bremen. He received the Dr. rer. nat. at the University of Bremen in 2015 with a dissertation on modeling and controlling the interaction of haptic human machine interfaces and robotic systems. In 2017, he has started working for the Institute of Robotics and Process Control (IRP) at the Technical University of Braunschweig. His research interests are in the fields of applied mathematics, geometry, mechanical analysis, and computer science.
- Marc Simnofske received the Dr.-Ing. in Mechanical Engineering from the Technical University of Braunschweig in 2009. Since 2010, he has been a Postdoctoral Researcher and Team Leader of the System Design team at the Robotics Innovation Center (RIC) of the German Research Center for Artificial Intelligence (DFKI GmbH) in Bremen. His research interests are in the field of mechanical design, robotics, mechatronics and parallel kinematic manipulators.
- Frank Kirchner studied computer science and neurobiology at the University Bonn, where he received the Dr. rer. nat. in computer science in 1999. Since 1994, he has been a Senior Scientist at the Gesellschaft für Mathematik und Datenverarbeitung (GMD) and, from 1998, at the Department for Electrical Engineering at Northeastern University. In 1999, he was appointed Tenure Track Assistant Professor at the Northeastern University, and since 2002 as a Full Professor at the University of Bremen. Since December 2005 he has been the CEO of the Robotics Innovation Center (RIC), and since 2013 Scientific Director of the Brazilian Institute of Robotics (BIR).